

1 **A grid dataset of leaf age-dependent LAI seasonality product (Lad-**
2 **LAI) over tropical and subtropical evergreen broadleaved forests**

3 Xueqin Yang^{1,2,3}, Xiuzhi Chen^{1,*}, Jiashun Ren^{1,4}, Wenping Yuan¹, Liyang Liu⁵, Juxiu
4 Liu⁶, Dexiang Chen⁷, Yihua Xiao⁷, Shengbiao Wu⁸, Lei Fan⁹, Xiaoi Dai⁴, Yunpeng
5 Wang³, and Yongxian Su²

6 ¹Guangdong Province Data Center of Terrestrial and Marine Ecosystems Carbon Cycle,
7 Guangdong Province Key Laboratory for Climate Change and Natural Disaster Studies,
8 School of Atmospheric Sciences, Sun Yat-sen University & Southern Marine Science
9 and Engineering Guangdong Laboratory (Zhuhai), Zhuhai 519082, China

10 ²Key Lab of Guangdong for Utilization of Remote Sensing and Geographical
11 Information System, Guangdong Open Laboratory of Geospatial Information
12 Technology and Application, Guangzhou Institute of Geography, Guangdong Academy
13 of Sciences, Guangzhou 510070, China

14 ³Guangzhou Institute of Geochemistry, Chinese Academy of Sciences, Guangzhou,
15 510640, China

16 ⁴College of Earth Sciences, Chengdu University of Technology, Chengdu 610000,
17 China;

18 ⁵Laboratoire des Sciences du Climat et de l'Environnement, IPSL, CEA-CNRS-UVSQ,
19 Université Paris-Saclay, 91191 Gif sur Yvette, France

20 ⁶Dinghushan Forest Ecosystem Research Station, South China Botanical Garden,
21 Chinese Academy of Sciences, Guangzhou 510650, China;

22 ⁷Pearl River Delta Forest Ecosystem Research Station, Research Institute of Tropical
23 Forestry, Chinese Academy of Forestry, Guangzhou 510650, China;

24 ⁸School of Biological Sciences, The University of Hong Kong, Pokfulam, Hong Kong

25 ⁹Chongqing Jinpo Mountain Karst Ecosystem National Observation and Research
26 Station, School of Geographical Sciences, Southwest University, Chongqing 400715,
27 China

28 * Correspondence: Xiuzhi Chen (chenxzh73@mail.sysu.edu.cn)

29 **Abstract**

30 Quantification of large-scale leaf age-dependent leaf area index has been lacking in
31 tropical and subtropical evergreen broadleaved forests (TEFs) despite the recognized
32 importance of leaf age in influencing leaf photosynthetic capacity in this biome. Here,
33 we simplified the canopy leaves of TEFs into three age cohorts (i.e., young, mature and
34 old one with different photosynthesis capacity ($V_{c,max}$)) and **proposed a novel neighbor-**
35 **based approach to develop** a first grid dataset of **monthly** leaf age-dependent LAI
36 product (**referred to as Lad-LAI**) **at 0.25-degree spatial resolution** over the continental
37 scale **during 2001-2018** from satellite observations of **sun-induced chlorophyll**
38 **fluorescence (SIF)** that was reconstructed from MODIS and TROPOMI (the
39 TROPOspheric Monitoring Instrument). The **new Lad-LAI products show good**
40 **performance in capturing the** seasonality of three LAI cohorts, i.e., young (LAI_{young})
41 ($R=0.36$), mature (LAI_{mature}) ($R=0.77$) and old (LAI_{old}) ($R=0.59$) leaves, at the eight
42 sites (**four in south America, three in subtropical Asia and one in Congo**) and can also
43 represent their interannual dynamics at the Barro Colorado site, with R being equal to
44 **0.54, 0.64 and 0.49** for LAI_{young} , LAI_{mature} and LAI_{old} , respectively. Additionally, the
45 **abrupt drops in LAI_{old} are mostly consistent with the seasonal litterfall peaks at 53 *in***
46 ***situ* measurements across the whole tropical region ($R=0.82$).** The LAI seasonality of
47 **young and mature leaves also agrees well with the seasonal dynamics of Enhanced**
48 **Vegetation Index (EVI) ($R=0.61$), which is a good proxy of effective leaves. Spatially,**
49 **the grid Lad-LAI captures** a dry-season green-up of canopy leaves across the wet
50 Amazonia areas where mean annual precipitation exceeds $2,000 \text{ mm yr}^{-1}$, consistent
51 with previous satellite-based analyses. The spatial patterns clustered from the three LAI
52 cohorts also coincide with those clustered from climatic variables over the whole TEF
53 region. The seasonality of LAI_{young} , LAI_{mature} and LAI_{old} derived from the estimated
54 GPP based on a simple linear SIF-GPP relationship show the highest correlation with
55 the *in situ* measurements at 8 observed sites compared with those derived from Orbiting
56 Carbon Observatory-2-based SIF (GOSIF) GPP and eddy covariance flux tower

57 measurements (FLUXCOM) GPP. Additionally, the Lad-LAI products developed by
58 the neighbor-based approach using 2*2 and 4*4 neighboring pixels show stable
59 seasonality in LAI_{young}, LAI_{mature} and LAI_{old} across the whole tropical region,
60 respectively. We provide the average seasonality of three LAI cohorts as the main
61 dataset, and their time-series as a supplementary dataset. These two products are
62 available at <https://doi.org/10.6084/m9.figshare.21700955.v3> (Yang et al., 2022).

63

64 **1. Introduction**

65 Tropical and subtropical evergreen broadleaved forests (TEFs) account for
66 approximately 34% of global terrestrial primary productivity (GPP) (Beer et al., 2010)
67 and 40-50% of the world's gross forest carbon sink (Pan et al., 2011; Saatchi et al.,
68 2011). Despite a perennial canopy, TEFs shed and rejuvenate their leaves continuously
69 throughout the year, leading to significant seasonality in canopy leaf demography (Wu
70 et al., 2016; Chen et al., 2021). This phenological changes in leaf demography is the
71 primary cause of GPP seasonality in TEFs (Saleska et al., 2003; Sayer et al., 2011; Leff
72 et al., 2012) and thus largely regulates their seasonal carbon sinks (Beer et al., 2010;
73 Aragao et al., 2014; Saatchi et al., 2011).

74 A key plant trait linking canopy phenology with GPP seasonality was shown to be
75 leaf age (Wu et al., 2017; Xu et al., 2017). At leaf scale, the newly-flushed young leaves
76 and maturing leaves show higher maximum carboxylation rates ($V_{c,max}$) than the old
77 leaves being replaced (De Weirdt et al., 2012; Chen et al., 2020). Such age-dependent
78 variations in $V_{c,max}$ is associated with changes in leaf nutritional contents (nitrogen,
79 phosphorus and potassium etc.) and stomatal conductance over time (Menezes et al.,
80 2021). Xu et al. (2017) and Menezes et al. (2021) monitored *in situ* leaf age and leaf
81 demography combined with leaf-level $V_{c,max}$ in Amazonian TEFs and found that $V_{c,max}$
82 of newly-flushed leaves increases rapidly with leaf longevity, peaks at approximately
83 2-month old and then declines gradually as leaf grows older (leaf age > 2 months). At
84 canopy scale, it was hypothesized that leaf demography and seasonal differences in leaf

85 age compositions of tree canopies control the GPP seasonality in TEFs (Wu et al., 2016;
86 Albert et al., 2018). Similar mechanism was also observed by the ground-based LiDAR
87 which showed an increasing trend in upper canopy leaf area index (LAI) during the dry
88 season, whereas a decrease in lower canopy LAI (more old leaves) (Smith et al., 2019).
89 Wu et al. (2016) classified canopy leaves of Amazonian TEFs into three leaf age cohorts
90 (young: 1-2 months, mature: 3-5 months and old: ≥ 6 months). LAI of young and mature
91 leaves increases during the dry seasons and consequently promotes dry-season canopy
92 photosynthesis. Based on above age-dependent $V_{c,max}$ at leaf scale (Xu et al., 2017) and
93 LAI seasonality of different leaf age cohorts at canopy scale (Wu et al., 2016), Chen et
94 al. (2020; 2021) developed a climate-triggered leaf litterfall and flushing model and
95 successfully represented the seasonality of canopy leaf demography and GPP at four
96 Amazonian TEF sites. Overall, leaf age-dependent LAI seasonality is one of the vital
97 biotic factors in influencing the GPP seasonality in TEFs (Wu et al., 2016; Chen et al.,
98 2020).

99 Although the leaf age-dependent LAI seasonality can be well documented at site
100 level using phenology cameras (Wu et al., 2016), it is still rarely studied and remains
101 unclear at the continental scale. The key causation is that leaf flushing and litterfall of
102 TEFs in different climatic regions experience different seasonal constraints of water
103 and light availability during recurrent dry and wet seasons (Brando et al., 2010; Chen
104 et al., 2020; Davidson et al., 2012; Xiao et al., 2005). Thus, the seasonal patterns of LAI
105 in different leaf age cohorts become very complex at the continental scale (Chen et al.,
106 2020; Xu et al., 2015). Satellite-based remote sensing (Saatchi et al., 2011, Guan et al.,
107 2015) and land surface model (LSM) technologies (De Weirdt et al., 2012; Chen et al.,
108 2020; 2021) are two commonly used approaches for detecting the spatial heterogeneity
109 of plant phenology at a large scale. However, for satellite-based studies, most optical
110 signals are saturated in TEFs due to the dense covered canopies and thus fail to capture
111 the seasonality of total LAI in TEFs, much less decompose the LAI into different leaf
112 age cohorts. These limitations prevent satellite-based studies from accurately

113 representing the age-dependent LAI seasonality. Moreover, most ESM models also
114 show poor performances in simulating the LAI seasonality in different leaf age cohorts
115 (De Weirdt et al., 2012; Chen et al., 2020). This is because that the underlying
116 mechanisms linking seasonal water and light availability with leaf flushing and litterfall
117 seasonality are currently highly debated and remain elusive at regional scale (Leff et al.,
118 2012; Saleska et al., 2003; Sayer et al., 2011). This vague notion imposes a challenge
119 for accurately modeling continental-scale GPP seasonality in most LSMs (Restrepo-
120 Coupe et al., 2017; Chen et al., 2021).

121 To fill the research gap, this study aims to produce a global grid dataset of leaf age-
122 dependent LAI seasonality product (Lad-LAI) over the whole TEF biomes from 2001
123 to 2018. For this purpose, we first simplified that canopy GPP was composed of three
124 parts that were produced from young, mature and old leaves, respectively. GPP was
125 then expressed as a function of the sum of the product of each LAI cohort (i.e., young,
126 mature and old leaves, denoted as LAI_{young} , LAI_{mature} , and LAI_{old} , respectively) and
127 corresponding net CO₂ assimilation rate (A_n , denoted as $A_{n_{young}}$, $A_{n_{mature}}$, and $A_{n_{old}}$ for
128 young, mature and old leaves, respectively) (**Equation 1**). Then, we proposed a novel
129 neighbor-based approach to derive the values of three LAI cohorts. It was hypothesized
130 that forests in adjacent four cells in the grid map exhibited consistent seasonality in
131 both GPP, and LAI cohorts (LAI_{young} , LAI_{mature} , and LAI_{old}). Based on this assumption,
132 we applied **Equation 1** to each pixel and combined the four equations of 2*2
133 neighboring pixels to derive the three LAI cohorts using a linear least-squares with
134 constrained method. A_n was calculated using the Farquhar-von Caemmerer-Berry
135 (FvCB) leaf photochemistry model (Farquhar et al., 1980); and GPP was linearly
136 derived from an arguably better proxy—TROPOMI (the TROPOspheric Monitoring
137 Instrument) Solar-Induced Fluorescence (SIF) based on a simple SIF-GPP relationship
138 established by Chen et al. (2022) (see **Methods** for details). This grid dataset of three
139 LAI cohorts provides new insights into tropical and subtropical phenology with more
140 details of sub-canopy level of leaf seasonality in different leaf age cohorts and will be

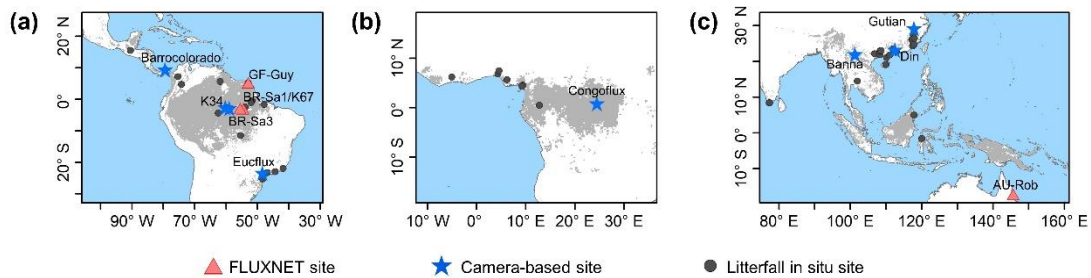
141 helpful for developing accurate tropical phenology model in ESMs.

142

143 2. Study area and material

144 2.1 Tropical and subtropical evergreen broadleaved forest biomes

145 In this study, we focused on the whole tropical and subtropical evergreen broadleaf
146 forests (TEFs). The pixels labeled TEFs according to the International Geosphere-
147 Biosphere Program (IGBP) classification were extracted as the study area based on the
148 0.05° spatial resolution MODIS land cover map (**Fig. 1**) (MCD12C1, Sulla-Menashe et
149 al., 2018). The study area contains three regions: South America (30°S–18°N; 40°W–
150 90°W), the world's largest and most biodiverse tropical rain forest, Congo (10°S–10°N;
151 10°W–30°E), the western part of the Africa TEF region, and Tropical Asia (20°S–30°N;
152 70°E–150°E), covering the Indo-China Peninsula, the majority of the Malay
153 Archipelago and the northern Australia.



154

155 **Figure 1.** Study areas over tropical and subtropical evergreen broadleaves forests (TEF).
156 Red triangles: observed GPP seasonality at four eddy covariance (EC) tower sites. Blue
157 pentangles: observed LAI cohorts at eight camera-based observation sites. Black circles:
158 observed litterfall seasonality at 53 observation sites.

159

160 2.2 Input datasets for calculating GPP and An parameters

161 The TROPOspheric Monitoring Instrument (TROPOMI) Solar-Induced
162 Fluorescence (SIF) data were used to derive the continent-scale GPP (denoted as
163 RTSIF-derived GPP) according to the SIF-GPP relationship established by Chen et al.
164 (2022) which used 15.343 as a transformation coefficient to covert SIF to GPP. The air

165 temperature data from ERA5-Land (Zhao, Gao et al., 2020), vapor pressure deficits
166 (VPD) data from ERA-Interim (Yuan et al., 2019) and downward shortwave solar
167 radiation (SW) from Breathing Earth System Simulator (BESS) (Ryu et al., 2018) were
168 used to calculate K_C , K_O , I^* , R_{dark} and $V_{c,max}$ and thus to calculate A_n according to
169 equations in **Table S4**. The calculation processes were illustrated in **Fig. 2**. All datasets
170 were aggregated at the same spatial (0.125°) and temporal resolutions (month) (**Table**
171 **S3**).

172

173 **2.3 Datasets for validating leaf age-dependent LAI seasonality**

174 **Ground-based seasonal LAI cohorts and litterfall data.** Top-of-canopy
175 imageries observed by ground-based phenology cameras were used to decompose
176 canopy LAI into LAI_{young} , LAI_{mature} and LAI_{old} . In total, imageries from eight
177 observation sites across the whole TEF region were used to validate the simulating
178 results (blue pentangles in **Fig. 1**, **Table S1**). Additionally, the seasonal litterfall data
179 from 53 *in situ* sites (black circles in **Fig. 1**, **Table S6**) spanning the TEFs were collected
180 from globally published articles to compare with the phase of simulated LAI_{old}
181 seasonality (see **Methods** for details). The multiyear monthly litterfall data were
182 averaged to the monthly mean to compare with the seasonality of simulated LAI_{old} .
183 Four eddy covariance flux tower sites (red triangles in **Fig. 1**, **Table S2**) provided *in*
184 *situ* seasonal GPP data to evaluate the seasonality of RTSIF-derived GPP.

185 **Satellite-based seasonal EVI data.** To evaluate the LAI seasonality of
186 photosynthesis-effective leaves, i.e., young and mature leaves, this study used satellite-
187 based MODIS Enhanced Vegetation Index (EVI) (Huete et al., 2002; Lopes et al., 2016;
188 Wu et al., 2018) as a remotely sensed proxies alternatives of effective leaf area changes
189 and new leaf flush, i.e., $LAI_{young+mature}$ (Wu et al., 2016; Xu et al., 2015). To prove the
190 robustness of the products over a large spatial coverage, the seasonal LAI cohorts of
191 young and mature leaves were evaluated against the enhanced vegetation index (EVI)
192 product, which was considered as a proxy for leaf area changes of photosynthetic

193 effective leaves (Xu et al., 2015; Wu et al., 2016; de Moura et al., 2017).

194

195 **3. Methods**

196 **3.1 Decomposing LAI cohorts (young, mature and old) from SIF-derived GPP**

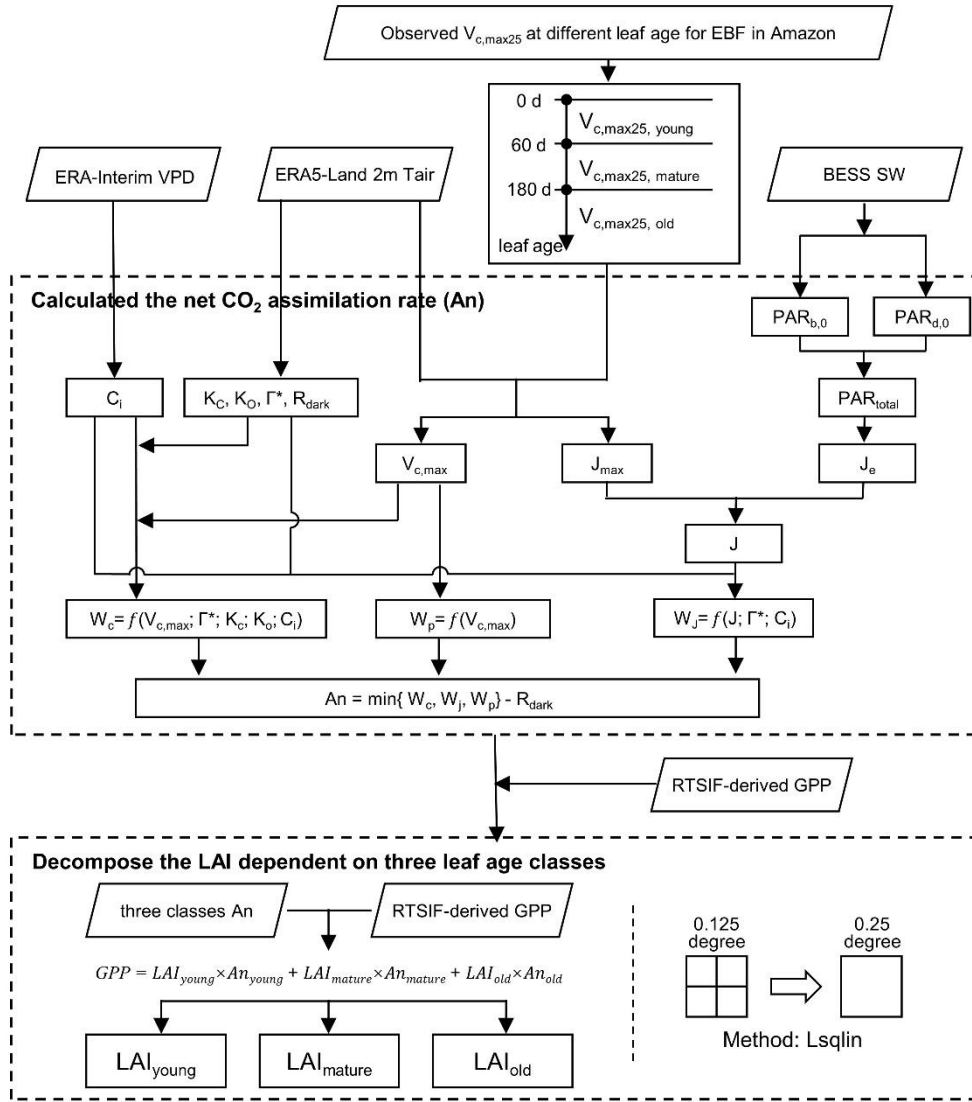
197 **Figure 2** illustrates the overall framework used to generate leaf age-dependent LAI
198 seasonality product (Lad-LAI). The majority of the tropical and subtropical EBFs retain
199 leaves year-round and their total LAI shows marginally small **spatial and** seasonal
200 changes (Wu et al., 2016) (**Figs. S3, S4**). Therefore, previous modelling studies have
201 assumed a constant value for the total LAI in tropical and subtropical EBFs (Cramer et
202 al., 2001; Arora and Boer, 2005; De Weirdt et al., 2012). **Based on this, we collected**
203 **observed seasonal LAI dynamics in tropical and subtropical EBFs from previously**
204 **published literatures which showed a constant value of LAI around 6.0 (Figs. S3, S4,**
205 **Table S5). Thus, in this study, we simplified to assume that the seasonal LAI was**
206 **approximately equaling to 6.0** in tropical and subtropical EBFs. We grouped the canopy
207 leaves of tropical and subtropical EBFs into three leaf age cohorts, i.e., young, mature
208 and old leaves, respectively. Then, the total GPP **was defined as** the sum of those
209 produced by the young, mature and old leaves, respectively. According to the Farquhar-
210 von Caemmerer-Berry (FvCB) leaf photochemistry model (Farquhar et al., 1980), GPP
211 can be expressed as function of the sum of the products of each LAI cohort (LAI_{young} ,
212 LAI_{mature} , and LAI_{old}) and corresponding net CO₂ assimilation rate (An_{young} , An_{mature} ,
213 and An_{old}) (**Equation 1**).

$$214 \quad GPP = LAI_{young} \times An_{young} + LAI_{mature} \times An_{mature} + LAI_{old} \times An_{old} \quad (1)$$

215 where LAI_{young} , LAI_{mature} and LAI_{old} are the leaf area index **of young, mature and old**
216 **leaves, respectively**; An_{young} , An_{mature} and An_{old} are the net rate of CO₂ assimilation
217 dependent on three leaf age classes; GPP is canopy total gross primary production. The
218 sum of LAI_{young} , LAI_{mature} and LAI_{old} **was set as a constant in this study**, equaling to **6.0**.

219 The **grid GPP data over the whole EBFs were** derived from SIF (denoted as RTSIF-
220 derived GPP) using a linear **SIF-GPP** regression model (see sect. 3.2) **which were**

221 established based on *in situ* GPP from 76 eddy covariance (EC) sites (Chen et al., 2022).
222 The $A_{n_{young}}$, $A_{n_{mature}}$ and $A_{n_{old}}$ were calculated according to the FvCB biochemical
223 model (Farquhar et al., 1980; Bernacchi et al., 2003) (see section 3.3). As there were
224 three unknown variables (i.e., LAI_{young} , LAI_{mature} and LAI_{old}) to be solved in Equation
225 1, we hypothesized that the adjacent four pixels exhibited homogenous EBFs and
226 consistent leaf demography and canopy photosynthesis. Then, we used the GPP and A_n
227 data from adjacent four pixels to estimate their LAI_{young} , LAI_{mature} and LAI_{old} based on
228 Equation 1 using a linear least-squares with constrained method. The inputs grid
229 datasets (i.e., RTSIF-derived GPP and A_n derived from T_{air} , VPD and SW) (Table S3,
230 Fig. 2) were sampled at 0.125-degree spatial resolution; while the output maps of
231 LAI_{young} , LAI_{mature} , and LAI_{old} were at 0.25-degree spatial resolution. Therefore, the
232 output maps of LAI_{young} , LAI_{mature} , and LAI_{old} were at a 0.25-degree spatial resolution.
233 Additionally, to test the robustness of the neighbor-based decomposition approach, we
234 increased the number of adjacent pixels from 4 ($2*2$) to 16 ($4*4$) to produce another
235 version of Lad-LAI products with spatial resolution of 0.5-degree. All our analyses
236 were conducted using the Python (version 3.7, <http://www.python.org>) and Matlab
237 (version R2019b) software.



238

239 **Figure 2.** The workflow for mapping Lad-LAI using the LsqLin method. LsqLin is the
 240 abbreviation of Linear least-squares solver with bounds or linear constraints. All the
 241 abbreviations were described in supplementary Tables S4.

242

243 3.2 Calculating the GPP (RTSIF-derived GPP) from TROPOMI SIF

244 Satellite-retrieved solar-induced chlorophyll fluorescence (SIF) is a widely used
 245 proxy for canopy photosynthesis (Yang et al., 2015; Dechant et al., 2020). Here, we
 246 used a long-term reconstructed TROPOMI SIF dataset (RTSIF) (Chen et al., 2022) to
 247 estimate GPP seasonality. Previous analyses showed that RTSIF was strongly linearly
 248 correlated to eddy covariance (EC) GPP and used 15.343 as a transformation coefficient

249 to covert RTSIF to GPP (Fig. 8a in Chen et al., 2022). In this study, we followed
250 previously published literatures to set a constant value of LAI around 6.0 for the whole
251 tropical and subtropical EBFs (Figs. S3, S4, Table S5). We collected seasonal GPP data
252 observed at four EC sites from the FLUXNET 2015 Tier 1 dataset (Table S2; Pastorello
253 et al., 2020) and validated the Chen's simple SIF-GPP relationship (Fig. S1). Results
254 confirmed the robustness of Chen's simple SIF-GPP relationship in estimating the GPP
255 seasonality in tropical and subtropical EBFs ($R > 0.49$). Despite potential overestimation
256 (Fig. S1 b) or underestimation (Fig. S1 h) of the magnitudes, RTSIF-derived GPP
257 mostly captured the seasonality of the EC GPP at all the four sites ($d_{\text{phase}} < 0.26$).

258

259 3.3 Calculating the net rate of CO₂ assimilation (An)

260 We calculated the net CO₂ assimilation (An) using the FvCB biochemical model
261 (Farquhar et al., 1980). In this model, the parameter An was calculated as the minimum
262 of Rubisco (W_c), RuBP regeneration (W_j) and TPU (W_p) to minus dark respiration (R_{dark})
263 (Bernacchi et al., 2013). The formulas for calculating An, W_c , W_j , W_p , R_{dark} and
264 corresponding intermediate variables were listed in Tables S4.

265 **Calculation of W_c .** W_c is expressed as a function of internal CO₂ concentration (c_i),
266 Michaelis-Menton constant for carboxylase (K_c), Michaelis-Menton constant for
267 oxygenase (K_o), CO₂ compensation point (Γ^*) and maximum carboxylation rate ($V_{c,\text{max}}$)
268 (Table S4-part1) (Lin et al., 2015; Bernacchi et al., 2013; Ryu et al., 2011; Medlyn et
269 al., 2011; June et al., 2004; Farquhar et al., 1980). The K_c , K_o , Γ^* and $V_{c,\text{max}}$ are
270 temperature-dependent variables. Thus, we used Equation 2 to calculate their values at
271 T_k by converting from those at 25°C. Then, we used the Medlyn's stomatal conductance
272 model (Medlyn et al., 2011) to estimate internal CO₂ concentration (c_i) (Equation 3),
273 which is expressed as a function of vapor pressure deficit (VPD) rather than relative
274 humidity (Lin et al., 2015). The method for calculating the $V_{c,\text{max}}$ of each LAI cohort
275 was introduced in section 3.4. The formulas for calculating corresponding intermediate
276 parameters were presented in Table S4.

277 $Para = Para_{25} \times \exp\left(\frac{(T_k - 298.15) \times \Delta H_{para}}{R \times T_k \times 298.15}\right)$ (2)

278 where *Para* denotes a correction factor arising from the temperature dependence of
 279 $V_{c,max}$; $Para_{25}$ are values of the temperature-dependent parameters (K_c , K_o , Γ^* and $V_{c,max}$)
 280 at the temperature 25°C; T_k denotes temperature in Kelvin; ΔH_{para} is the activation
 281 energy for temperature dependence; R is the universal gas constant.

282 $c_i = c_a \times \left(1 - \frac{1}{1.6 \times \left(1 + \frac{g_1}{\sqrt{VPD}}\right)}\right)$ (3)

283 where c_a is atmospheric CO₂ concentration, 380 ppm; VPD is calculated from air
 284 temperature and dew point temperature of the global ERA-Interim reanalysis dataset
 285 (Dee et al., 2011) using the method of Yuan et al. (2019). The calculation formula of
 286 VPD was described in supplementary files. In this study, we used the value of 3.77 for
 287 the stomatal slope (g_1) in the stomatal conductance model according to Lin et al. (2015).

288 **Calculation of W_p .** W_p was calculated as the function of $V_{c,max}$, which were given
 289 different values for different LAI cohorts based on multiple *in situ* observations (section
 290 3.4).

291 **Calculation of W_j .** W_j was calculated from $V_{c,max}$, c_i and the rate of electrons
 292 through the thylakoid membrane (J) (Bernacchi et al., 2013). The parameter J was
 293 calculated from maximum electron transport rate (J_{max}) and the rate of whole electron
 294 transport provided by light (J_e) (Bernacchi et al., 2013). J_{max} was expressed as a
 295 temperature dependence function of maximum electron transport rate ($J_{max,25}$) at 25°C
 296 and temperature (T_{air}) and J_e was expressed as a function of total PAR absorbed by
 297 canopy (PAR_{total}) that was the sum of active radiation in beam ($PAR_{b,0}$) and diffuse
 298 ($PAR_{d,0}$) light firstly (Weiss et al., 1985), which were calculated from downward short-
 299 wave radiation (SW) (Ryu et al., 2018). The formula for PAR_{total} was given in **Equation**
 300 **4** and formulas for other intermediate parameters (i.e., $PAR_{b,0}$, $PAR_{d,0}$, ρ_{cb} , ρ_{cd} , k'_b , k'_d ,
 301 and CI) were listed in **Table S4**.

302 $PAR_{total} = (1 - \rho_{cb}) \times PAR_{b,0} \times (1 - \exp(-k'_b \times CI \times LAI_{total})) + (1 - \rho_{cd}) \times$
 303 $PAR_{d,0} \times (1 - \exp(-k'_d \times CI \times LAI_{total}))$ (4)

304 where PAR_{total} is total PAR absorbed by canopy; $PAR_{b,0}$ is the active radiation; $PAR_{d,0}$
305 is diffuse radiation; LAI_{total} is a total LAI. Here, we used a constant value of 6.0
306 according to De Weirdt et al. (2012).

307

308 **3.4 Classifying three LAI cohorts with different $V_{c,max}$**

309 In this study, we collected *in situ* samples of $V_{c,max25}$ data against different leaf age
310 across tropical and subtropical EBFs from previous publications. Mature leaves (leaf
311 age: 70-160 days) show highest $V_{c,max25}$ than those of new flushed leaves (leaf age: <60
312 days) and old leaves(leaf age: >200 days) as Menezes et al. (2021). Therefore, in this
313 study, we classified the canopy leaves into three cohorts: young (leaf age: <2 months),
314 mature (leaf age: 3-5 months) and old cohorts (leaf age: >6 months) as Wu et al. (2016).
315 The $V_{c,max25}$ for young, mature and old cohorts were set as 60, 40 and 20 $\mu\text{mol m}^{-2} \text{s}^{-1}$,
316 respectively, according to previous ground-based observations by Chen et al. (2020).

317

318 **3.5 Decomposing camera-based LAI into three leaf age cohorts**

319 We classified the canopy leaves into young, mature and old age cohorts based on
320 the green-color band from the top-of-canopy imageries observed by RGB camera. It is
321 because that the brightness of different leaf age leaves differs greatly in the values of
322 green-color band. Raster density slicing is a useful classification method for detecting
323 the attributes of various ground objects (Kartikeyan et al., 1998). Therefore, we set three
324 brightness thresholds to divide young (blue), mature (green), old (yellow) leaves and
325 background (gray) for the same canopy extent in each month (Fig. S2). This analysis
326 was conducted in ENVI5.3 software.

327

328 **3.6 Evaluating the $LAI_{young+mature}$ seasonality and its spatial patterns using** 329 **satellite-based EVI products**

330 To compare the seasonality of $LAI_{young+mature}$ with those of EVI, we calculate mean
331 squared deviation (MSD) and their three components— d_{bias} , which denotes the

332 differences about absolute value, d_{var} , which denotes the differences of seasonal
333 fluctuations, and d_{phase} , which denotes the differences of peak phase to evaluate this
334 consistence, comprehensively (see section 3.8). Additionally, we compared the spatial
335 patterns of the wet- minus dry-season differences (Δ) between observed and simulated
336 variables, following the work of Guan et al. (2015). To determine the wet and dry
337 seasons in each grid cell, we defined a month as dry one when its monthly average
338 precipitation was smaller than the potential evapotranspiration (PET) computed using
339 the method of Maes et al. (2019); other months were classified as wet ones. The wet-
340 minus dry-season $LAI_{young+mature}$ (denoted as $\Delta LAI_{young+mature}$) was calculated for each
341 grid cell as the wet-season average $LAI_{young+mature}$ value minus the dry-season average
342 value of $LAI_{young+mature}$.

343

344 **3.7 Evaluating the LAI_{old} seasonality using ground-based litterfall data**

345 Litterfall is closely related to the seasonal dynamics of old leaves, i.e., LAI_{old} (Chen
346 et al., 2020; Yang et al., 2021). Previous analyses indicated that, in general, a sharpening
347 decrease in LAI_{old} corresponded to a peak in litterfall (Pastorello et al., 2020; Midoko
348 Iponga et al., 2019; Ndakara, 2011; Barlow et al., 2007; Dantas and Phillipson, 1989).
349 Based on this causal relationship between litterfall and LAI_{old} , we compared the time
350 of seasonal litterfall peak with the time of abrupt drops in LAI_{old} , to indirectly evaluate
351 the simulated LAI_{old} seasonality. To accurately detect the onset date of old leaves
352 shedding and the day of litterfall peak, we used a least-square regression analysis
353 method developed by Piao et al. (2006) to smoothen LAI_{old} and litterfall seasonal curves.
354 The sixth-degree polynomial function ($n=6$) was applicable to the regression (**Equation**
355 **5**).

$$356 LAI_{old} = a_0 + a_1x + a_2x^2 + a_3x^3 + a_4x^4 + a_5x^5 + a_6x^6 \quad (5)$$

357 where x is the day of a year.

358 The slope of seasonal LAI ($LAI_{old, ratio}$) was calculated in **Equation 6**. The date of
359 abrupt drops in LAI_{old} was defined as the time with most negative values of $LAI_{old, ratio}$.

$$LAI_{old, ratio(t)} = (LAI_{old(t+1)} - LAI_{old(t)}) / (LAI_{old(t)}) \quad (6)$$

where $LAI_{old, ratio}$ is the slope of seasonal LAI_{old} curve. $LAI_{old(t+1)}$ and $LAI_{old(t)}$ are the corresponding monthly LAI at time t+1 and t, respectively.

363

3.8 Evaluation Metrics

Two metrics were chosen to evaluate the seasonality of Lad-LAI against the that of other proxies: the Kobayashi decomposition of the Mean Square Difference between model and observation (Kobayashi and Salam, 2000) and the Pearson correlation coefficient (Pearson, 1896) for gridded fields.

Mean squared deviation (MSD). The mean squared deviation (MSD) was given by Kobayashi and Salam (2000):

$$MSD = \frac{1}{n} \sum_{i=1}^n (x_i - y_i)^2 \quad (7)$$

$$SB = (\bar{x} - \bar{y})^2 \quad (8)$$

$$SD_s = \sqrt{\frac{1}{n} \sum_{i=1}^n (x_i - \bar{x})^2} \quad (9)$$

$$SD_m = \sqrt{\frac{1}{n} \sum_{i=1}^n (y_i - \bar{y})^2} \quad (10)$$

$$SDSD = (SD_s - SD_m)^2 \quad (11)$$

$$LCS = 2SD_s SD_m (1 - r) \quad (12)$$

where mean squared deviation is the square of RMSD; i.e., $MSD = RMSD^2$; and x_i is the simulated data at time t, and y_i is the observed one at time t (month). The lower the value of MSD, the closer the simulation is to the measurement. MSD can be decomposed into the sum of three components: the squared bias (d_{bias}), $d_{bias}=SB$; the squared difference between standard deviations (variance-related difference, d_{var}), $d_{var}=SDSD$; and the lack of correlation weighted by the standard deviations (phase-related difference, d_{phase}), $d_{phase}=LCS$; r indicates the correlation coefficient between x and y .

Pearson correlation coefficient (R). The Pearson correlation coefficient is a measure of linear correlation between two variables (Merkl and Waack, 2009). The

387 correlation coefficient between X and Y was as:

$$388 \rho_{X,Y} = \frac{cov(X,Y)}{\sigma_X \sigma_Y} = \frac{E((X-\mu_X)(Y-\mu_Y))}{\sigma_X \sigma_Y} \quad (13)$$

389

390 **3.9 The quality control (QC) for the Lad-LAI product**

391 To warn potential uncertainties, we provided information of data quality control
392 (QC) along with the Lad-LAI product (**Fig. S5**). In the QC system (**Table S7**), data
393 quality was divided into four levels: level 1 represents the highest quality; level 2 and
394 level 3 represent good and acceptable quality, respectively; and level 4 warns to be used
395 cautiously. This QC product was generated according to residual sum of squares (RSS)
396 (Melgosa et al., 2008) obtained from the constrained least-squares method that was used
397 to estimate derive monthly Lad-LAI data.

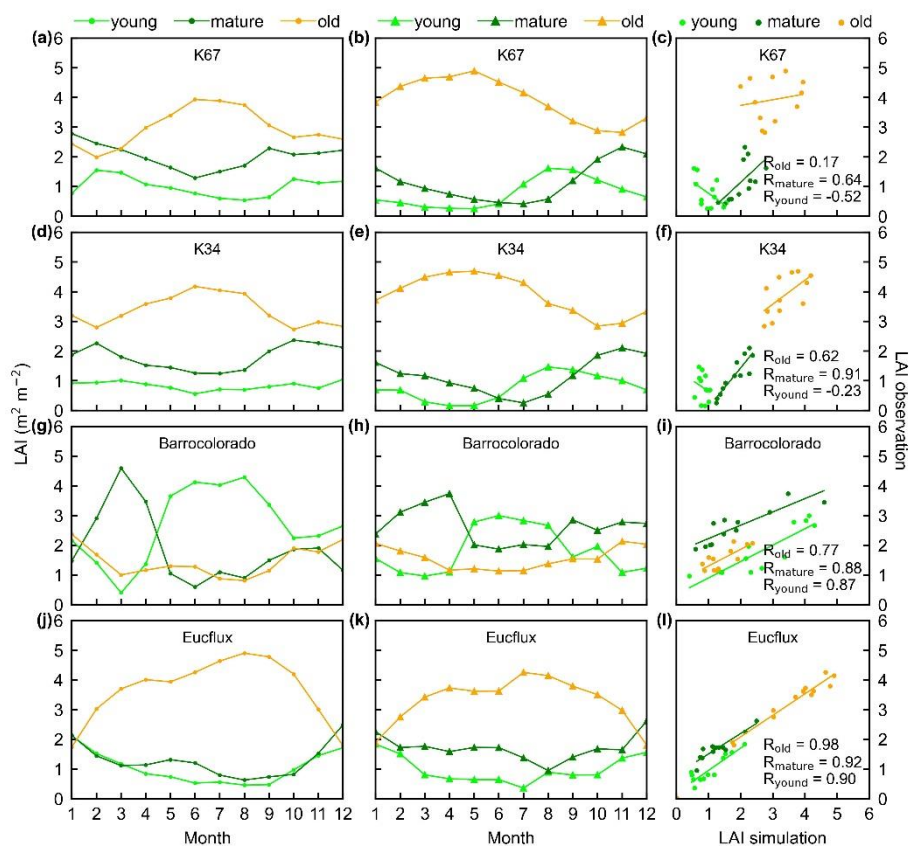
398

399 **4. Results**

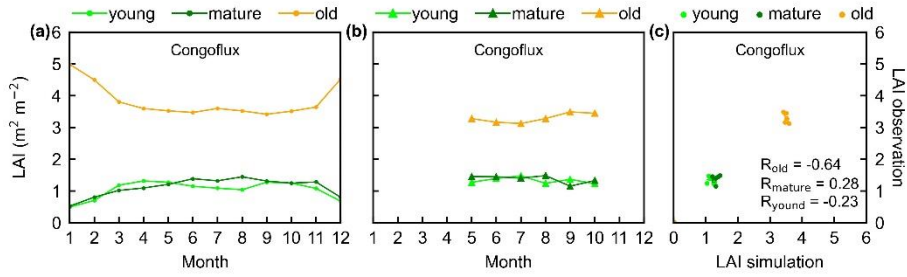
400 **4.1 Comparison of LAI cohort seasonality with sparse site observations**

401 The simulated leaf age-dependent LAI seasonality product was validated against
402 the camera-based measurements of LAI_{young}, LAI_{mature}, and LAI_{old} at four sites in south
403 America, one site in Congo and three sites in China. Overall, the LAI seasonality of
404 mature and old classes from the new Lad-LAI products agrees well at these sites with
405 very fine-scale collections of monthly LAI of mature (R=0.77, MSD=0.69) and old
406 leaves (R=0.59, MSD=0.62). However, the seasonality of simulated LAI from young
407 leaves performs a little poor (R=0.36, MSD=0.45). It is also interesting to note that the
408 canopy leaf phenology of TEFs at these sites differ greatly. In south America, at K67,
409 K34 and Eucflux sites, both *in situ* and simulated LAI_{young} and LAI_{mature} decrease at
410 early dry season around February and convert to increase at early wet season around
411 June (**Fig. 3 a, b, d, e, j, k**). At the Barrocolorado site, LAI_{young} increases from the late
412 dry to early wet season around Mar in response to the increasing incoming shortwave
413 radiation and in contrast, LAI_{mature} starts to increase at wet season around June (**Fig. 3**
414 **g, h**). However, in subtropical Asia, LAI_{young} and LAI_{mature} increase during the wet

415 season and peak with largest rainfall at June or July at Din, Gutian and Banna sites (**Fig.**
 416 **5 a, b, d, e, g, h**). In Congo, we only found one site (Congoflux) with six months
 417 observation period (from May to October). The seasonality of LAI_{young} and LAI_{mature}
 418 are similar as those in tropical Asia while having smaller variations in magnitude due
 419 to the moderate seasonality of sunlight the Equator region (**Fig. 4 a, b**). Overall, there
 420 is a reverse pattern for LAI_{old} seasonality compared to LAI_{mature} for all the **eight** sites.
 421

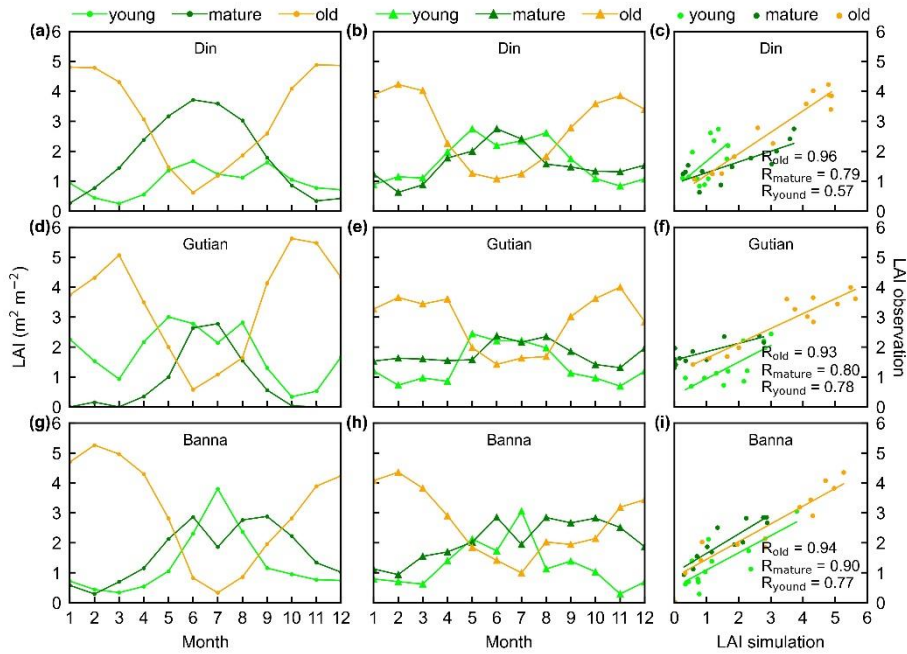


422
 423 **Figure 3.** Seasonality of simulated LAI_{young} , LAI_{mature} , and LAI_{old} in comparison with
 424 observed data at 4 sites in south America. (Panels a, d, g and j) simulated LAIs;
 425 (panels b, e, h and k) observed LAIs; (panels c, f, i and l) scatterplots between
 426 simulated and observed LAIs. Limegreen dots are LAI_{young} ; green dots are LAI_{mature} ;
 427 orange dots are LAI_{old} .



428

429 **Figure 4.** Seasonality of simulated LAI_{young} , LAI_{mature} , and LAI_{old} in comparison with
 430 observed data at one site in Congo. (a) Simulated LAIs; (b) observed LAIs; and (c)
 431 scatterplots between simulated and observed LAIs. Limegreen dots are LAI_{young} ;
 432 green dots are LAI_{mature} ; orange dots are LAI_{old} .



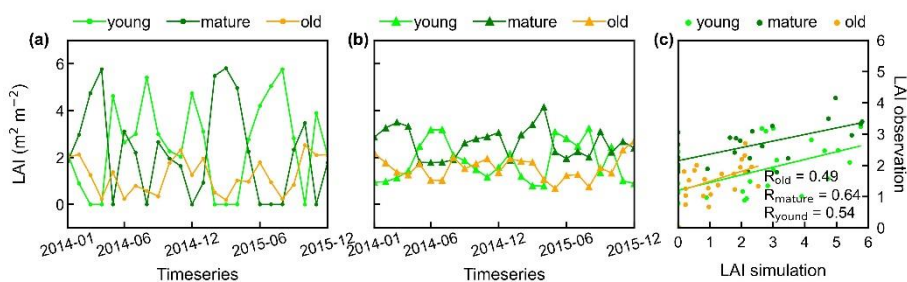
433

434 **Figure 5.** Seasonality of simulated LAI_{young} , LAI_{mature} , and LAI_{old} in comparison with
 435 observed data at 3 sites in tropical Asia. (Panels a, d and g) simulated LAIs; (panels b,
 436 e and h) observed LAIs; (panels c, f and i) scatterplots between simulated and observed
 437 LAIs. Limegreen dots are LAI_{young} ; green dots are LAI_{mature} ; orange dots are LAI_{old} .

438

439 Additionally, only one ground site (Barrocolorado site in Panama) had time-series
 440 camera-based phenological imageries, which was then used to evaluate capacity of Lad-
 441 LAI in representing the interannual dynamics of three LAI cohorts, with R values being
 442 equal to 0.54, 0.64, 0.49 for LAI_{young} , LAI_{mature} , LAI_{old} , respectively (Fig. 6). However,

443 more *in situ* long-term observations are in need to test the robustness of the time-series
 444 variations. The temporal variations of LAI_{young} , LAI_{mature} , LAI_{old} across 8 sub-regions
 445 classified by the *K*-means clustering analysis were shown in **Fig. S6**. Results showed
 446 that, for example, the LAI_{mature} increased significantly due to 2015 drought in Amazon
 447 basin (e.g., sub-region S2, **Fig. S6**) and southeast Asia (e.g., sub-region S7, **Fig. S6**),
 448 indicating good capability of detecting the dynamics of LAI_{young} , LAI_{mature} , LAI_{old} in
 449 response to climate disturbances.



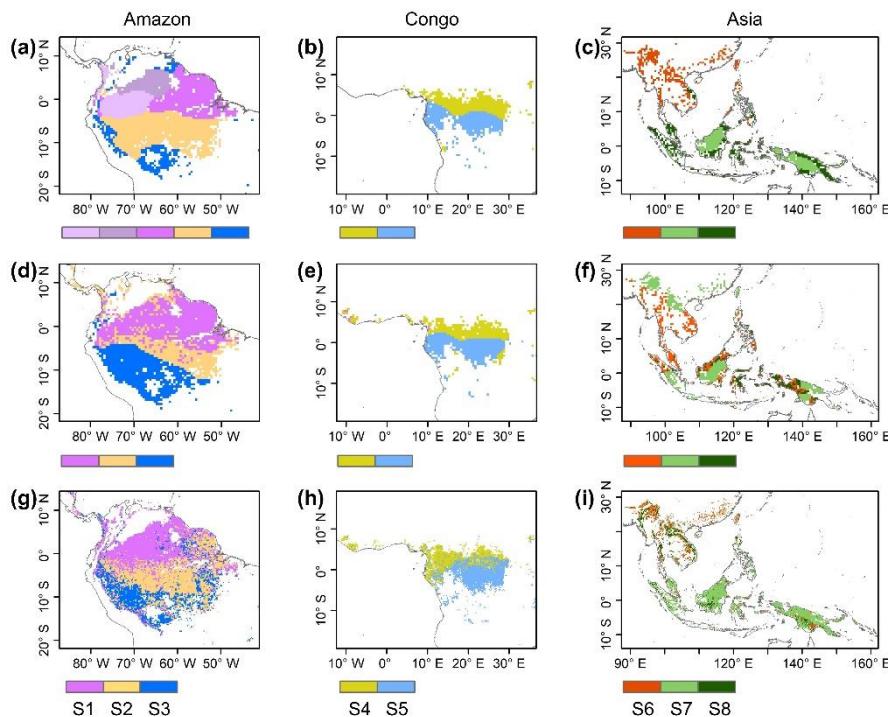
450
 451 **Figure 6.** Timeseries of simulated LAI_{young} , LAI_{mature} , and LAI_{old} in comparison with
 452 observed data at Barro Colorado site in Panama. (a) Simulations LAIs; (b) observation
 453 LAIs; and (c) scatterplots between simulated and observed LAIs.

455 4.2 Comparison of patterns of grid LAI cohort seasonality with previous climatic 456 and phenological patterns

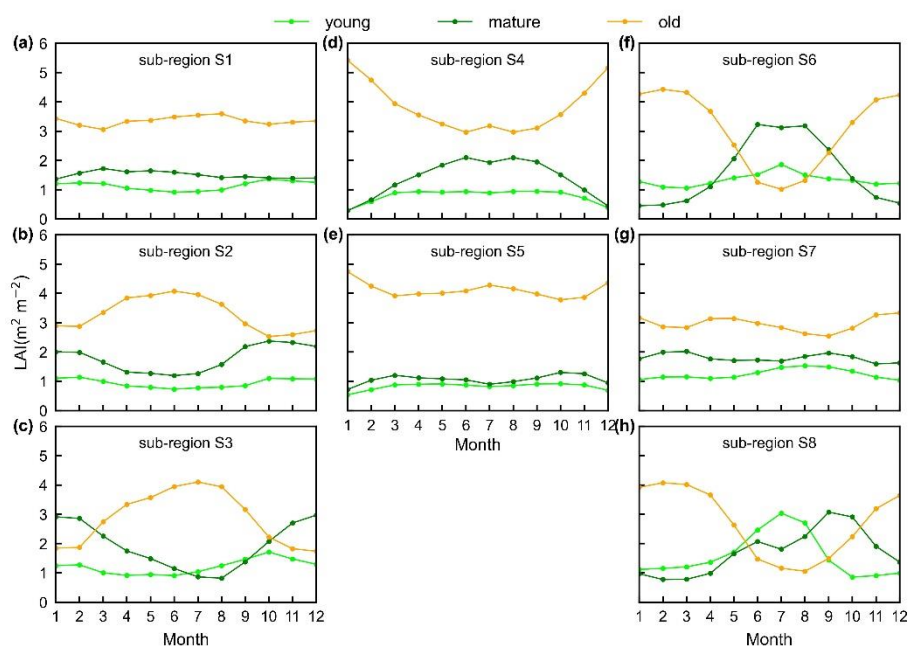
457 The *in situ* measurements of LAI_{young} , LAI_{mature} , and LAI_{old} suggested diverse
 458 patterns of Lad-LAI seasonality over the TEFs. Nevertheless, the sparse coverage of
 459 these sites raised challenging for a comprehensive and direct evaluation of leaf age-
 460 dependent LAI seasonality product. To continue the grid Lad-LAI seasonality product
 461 at the regional scale, we further conducted spatial clustering analyses of LAI_{young} ,
 462 LAI_{mature} , and LAI_{old} using the *K*-means analysis method.

463 Surprisingly, the spatial patterns of Lad-LAI product clustered from satellite-based
 464 vegetative signals (**Fig. 7 g-i**) coincide well with those clustered from in-dependent
 465 climatic variables (rainfall and radiation etc.) (**Fig. 7 a-c**). These patterns are also
 466 similar as those of the climate-phenology rhythms mapped by Yang et al. (2021), which
 467 suggest different correlations of litterfall seasonality with canopy phenology between

468 different climate-phenology rhythms (**Fig. 7 d-f**). In central (sub-region S2) and south
 469 (sub-region S3) Amazon (**Fig. 7 g**), the seasonality of LAI_{young}, LAI_{mature}, and LAI_{old}
 470 (**Fig. 8 b, c**) are similar as those of BR-Sa1 and BR-Sa3 sites. And in subtropical Asia
 471 (sub-region S6) (**Fig. 7 i**), the seasonality of three LAI cohorts (**Fig. 8 f**) are similar as
 472 those of Din, Gutian and Banna sites. Notably, the sub-region S8, located
 473 geographically between sub-regions S6 and S7, shows a LAI_{young} peak at July and a
 474 bimodal phenology in LAI_{mature} (**Fig. 8 h**). The remaining 4 sub-regions (sub-regions
 475 S1, S4, S5, S7) are all located nearby the equator. The magnitudes of seasonal changes
 476 in LAI cohorts are smaller than those in sub-regions S2, S3, S6 and S8 away from the
 477 Equator. It is worth noting that for these sub-regions around the Equator there is a
 478 bimodal seasonality pattern for LAI_{mature}, with the first peak around March and the
 479 second peak around August (**Fig. 8 a, d, e, g**). This is consistent with the findings of Li
 480 et al. (2021) which found that tropical and subtropical TEFs changed from a unimodal
 481 phenology at higher-latitudes to a bimodal phenology at lower-latitudes.



482
 483 **Figure 7.** Comparison of sub-regions of Lad-LAI products (plots g-i) with those of
 484 climatic factors classified by the K-means clustering analysis (plots a-c) (Chen et al.,
 485 2021) and those of the three climate-phenology regimes (plots d-f) developed by Yang



487

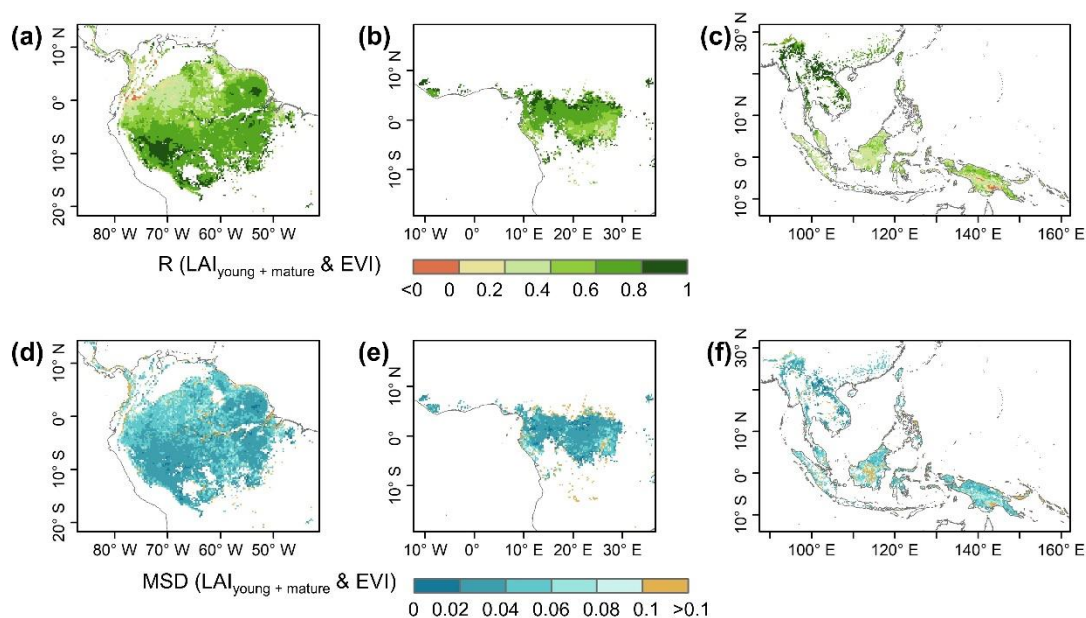
488 **Figure 8.** Seasonality of simulated LAI_{young} , LAI_{mature} , and LAI_{old} in 8 sub-regions
 489 classified by the K-means clustering analysis.

490

491 **4.3 Sub-regional evaluations of grid $LAI_{young+mature}$ seasonality using satellite-based** 492 **EVI products**

493 The grid dataset of $LAI_{young+mature}$ seasonality was indirectly evaluated using the
 494 satellite-based EVI products (Wang et al., 2017; de Moura et al., 2017; Xiao et al., 2005;
 495 Wu et al., 2018), as previous studies indicated that EVI can be considered as a proxy
 496 for leaf area change of those leaves with high photosynthesis efficiency (Huete et al.,
 497 2006; Lopes et al., 2016; Wu et al., 2018). It is because that EVI are very sensitive to
 498 changes in near-infrared (NIR) reflectance (Galvão et al., 2011) while young and
 499 mature leaves also reflect more NIR signals than the older leaves they replace (Toomey
 500 et al., 2009). The linear correlation and MSD decompositions (see **methods**) between
 501 simulated and satellite-based EVI were displayed in **Fig. 9**. Overall, the seasonal
 502 $LAI_{young+mature}$ is well correlated with satellite-based EVI ($R > 0.40$) in 78.26% of the
 503 TEFs and the average correlation coefficient is equaling to 0.61(**Fig. 9 a-c**). The MSD
 504 is smaller than 0.1 in 89.69% of the whole tropical and subtropical TEFs (**Fig. 9 d-f**).

505 Statistics in the 8 clustered sub-regions show that the seasonal $LAI_{young+mature}$ of Lad-
506 LAI data mostly correlate better with seasonal EVI in high-latitude areas (sub-region
507 S2: $R=0.65$, sub-region S3: $R=0.71$, sub-region S6: $R=0.67$) than those in low latitudes
508 (sub-region S1: $R=0.46$, sub-region S5: $R=0.61$, sub-region S7: $R=0.44$, sub-region S8:
509 $R=0.64$) except for sub-region S4 ($R=0.72$) (Figs. 10, S7). The MSD components also
510 confirm the better performance of $LAI_{young+mature}$ seasonality in high-latitude areas (sub-
511 region S2: $d_{bias}=0.009$, $d_{var}=0.001$, $d_{phase}=0.030$; sub-region S3: $d_{bias}=0.009$, $d_{var}=0.002$,
512 $d_{phase}=0.030$; sub-region S6: $d_{bias}=0.016$, $d_{var}=0.005$, $d_{phase}=0.040$) than in low-latitude
513 areas near the Equator (sub-region S1: $d_{bias}=0.012$, $d_{var}=0.001$, $d_{phase}=0.041$; sub-region
514 S4: $d_{bias}=0.020$, $d_{var}=0.001$, $d_{phase}=0.031$; sub-region S5: $d_{bias}=0.017$, $d_{var}=0.001$,
515 $d_{phase}=0.032$; sub-region S7: $d_{bias}=0.018$, $d_{var}=0.002$, $d_{phase}=0.043$; sub-region S8:
516 $d_{bias}=0.012$, $d_{var}=0.005$, $d_{phase}=0.035$) (Figs. 11, S7). This happens because that the
517 accuracy of Lad-LAI in representing the seasonality of LAI cohorts depends highly on
518 that of input SIF data, which is low sensitive to canopy phenology and shows
519 marginally small seasonal changes nearby the Equator, for example in tropical Asia
520 (Guan et al., 2015; 2016).



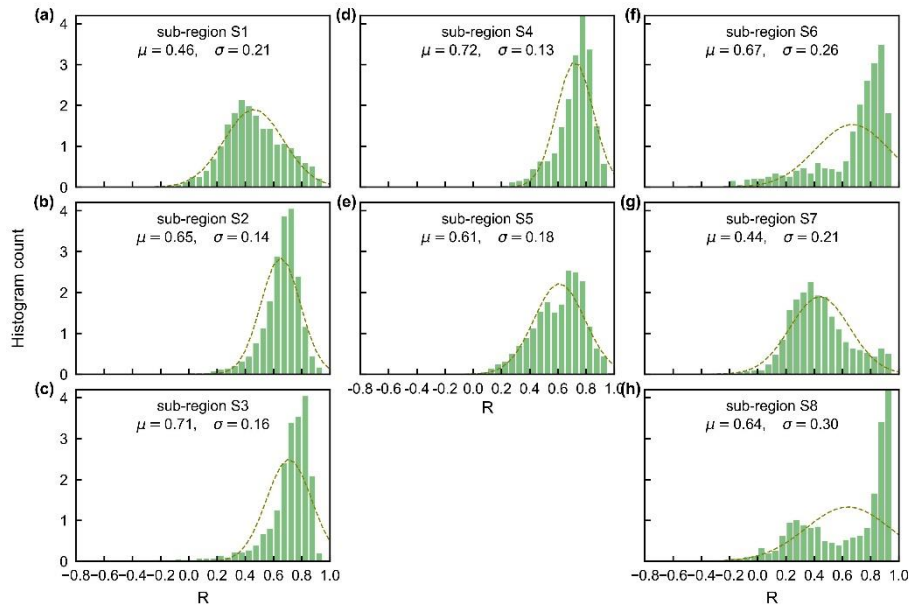
521

522 **Figure 9.** Pearson correlation coefficient (R) and mean squared deviation (MSD)

523 between seasonality of simulated $LAI_{young+mature}$ and MODIS Enhanced Vegetation

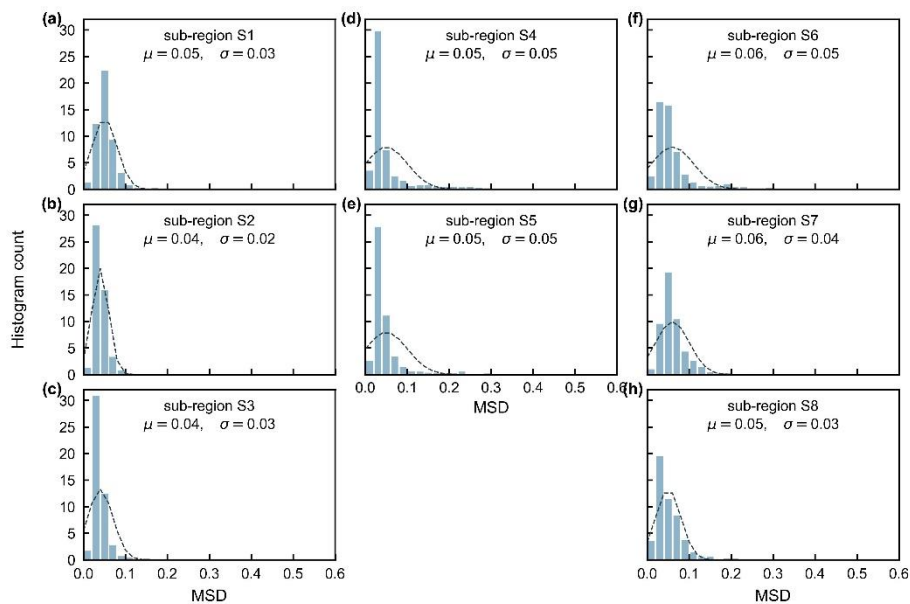
524 Index (EVI).

525



526

527 **Figure 10.** Statistics of the Pearson correlation coefficient (R) between seasonality of
528 simulated LAI_{young+mature} and MODIS Enhanced Vegetation Index (EVI) in the 8
529 clustered sub-regions.



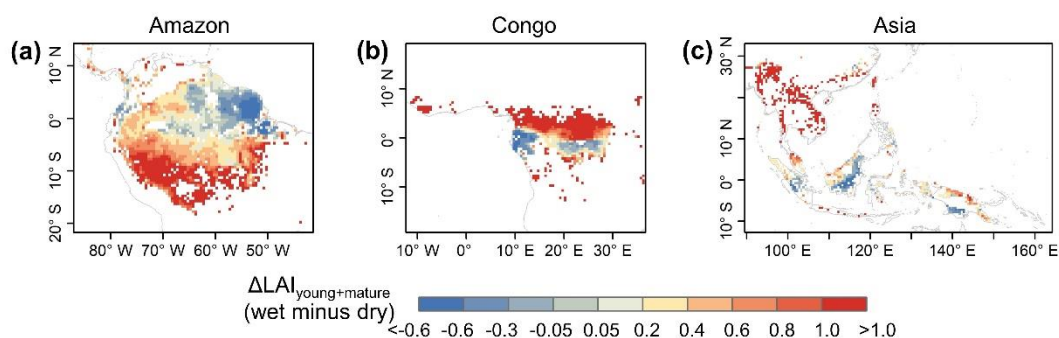
530

531 **Figure 11.** Statistics of the mean squared deviation (MSD) between seasonality of
532 simulated LAI_{young+mature} and MODIS Enhanced Vegetation Index (EVI) in the 8
533 clustered sub-regions.

534

535 Additionally, previous studies indicated large-scale dry-season green-up area over

536 tropical and subtropical region (i.e., Guan et al., 2015, Tang et al., 2017, Myneni et al.,
 537 2007) where the average annual precipitation exceeds 2,000 mm yr⁻¹. Here, we
 538 calculated the differences (Δ) between wet- and dry-season LAI_{young+mature} (i.e.,
 539 LAI_{young}+ LAI_{mature}), to test whether the Lad-LAI can capture this green-up spatial
 540 pattern. Spatial patterns of Δ LAI_{young+mature} (**Fig. 12**) are similar to those developed by
 541 (Guan et al., 2015), with higher LAI_{young+mature} during the dry season (blue area) in large
 542 areas north of the Equator. This indicates an emergence of new leaf flush and increase
 543 of mature leaves, resulting the canopy “green-up” phenomenon observed by previous
 544 satellite-based signals. It is interesting to note that the total areas (blue regions in **Fig.**
 545 **12**) of this dry-season green up shown by LAI_{young+mature} is smaller than those shown by
 546 SIF signals that almost everywhere north of the Equator. That is because that new and
 547 mature leaves often have quite a higher photosynthetic capacity than old leaves. A slight
 548 or moderate “green-up” in new and mature leaves (i.e., increase in LAI_{young+mature})
 549 would boost strong increase in photosynthesis, inducing significant “green-up” shown
 550 by photosynthesis-related signals, e.g., SIF data. Therefore, photosynthesis proxies
 551 likely overestimate the areas with “green-up” of new leaves during the dry seasons in
 552 the real world.



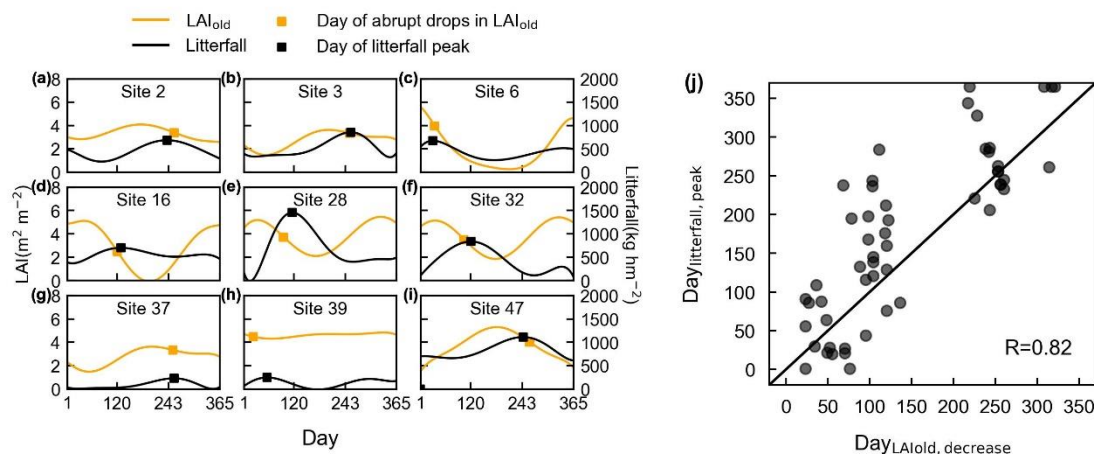
553
 554 **Figure 12.** Spatial pattern of dry-season green-up using wet-season LAI_{young+mature}
 555 minus dry-season LAI_{young+mature}.

556

557 **4.4 Sub-regional evaluations of grid LAI_{old} seasonality using site-based litterfall** 558 **observations**

559 The seasonal patterns of LAI_{old} were evaluated indirectly using ground-based

560 seasonal litterfall observations from 53 sites over the tropical and subtropical EBFs
 561 (black circles in Fig. 1, Figs. S8-S10), Here, we selected 9 specific sites (Fig. 13) with
 562 different patterns of litterfall seasonality and LAI_{old} seasonality, to illustrate the
 563 analyses results. Fig. 13 a-i illustrate the days when there is an abrupt decrease in
 564 monthly LAI_{old}, which are closely to monthly litterfall peak. The days when LAI_{old}
 565 decreases sharpest (Day_{LAIold}) agree well with the days when their monthly litterfall
 566 peaks (Day_{litterfall}) (Fig. 13 j), mostly distributed near the diagonal lines (R=0.82). This
 567 validation from seasonal litterfall data indirectly demonstrate the robustness of the
 568 LAI_{old} seasonality of the Lad-LAI product.



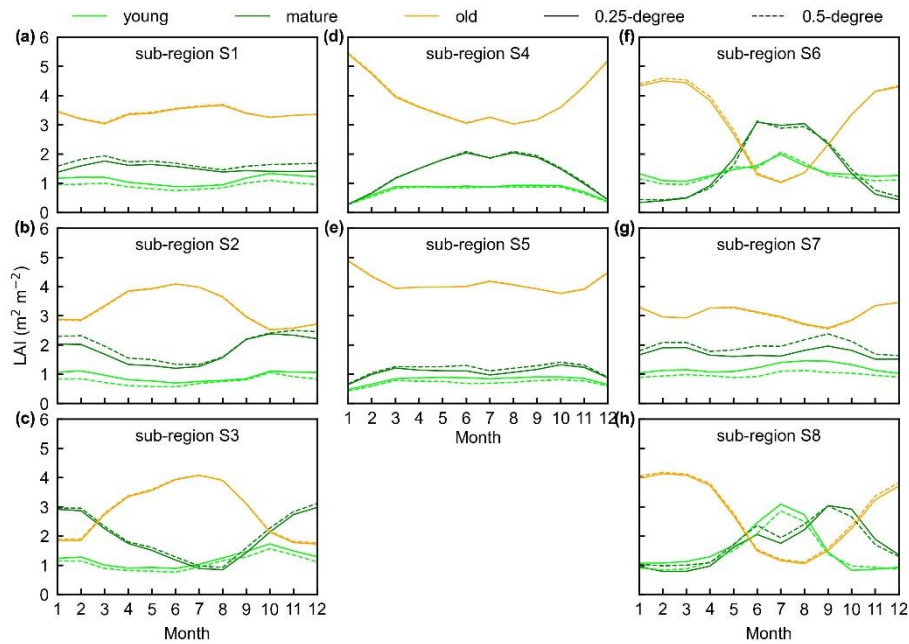
569
 570 **Figure 13.** Evaluation of simulated LAI_{old} using ground-observed litterfall seasonality.
 571 (a-i) Days of an abrupt decrease in LAI_{old} in comparison with days of corresponding
 572 litterfall peak at 9 specific sites for examples. The orange curves represent simulated
 573 LAI_{old}. Dots on the orange curves represent the point with an abrupt decrease in LAI_{old}.
 574 The black curves represent observed seasonal litterfall mass. The dots on the black
 575 curves represent the point with litterfall peak. (j) Comparisons of the days when LAI_{old}
 576 has an abrupt decrease (Day_{LAIold}) against the days when monthly litterfall peaks
 577 (Day_{litterfall}).

578

579 4.5 Testing potential uncertainties of the Lad-LAI products

580 To prove the robustness of the neighbor-based decomposition approach, we
 581 compared the Lad-LAI products generated based on 2*2 neighboring pixels with those

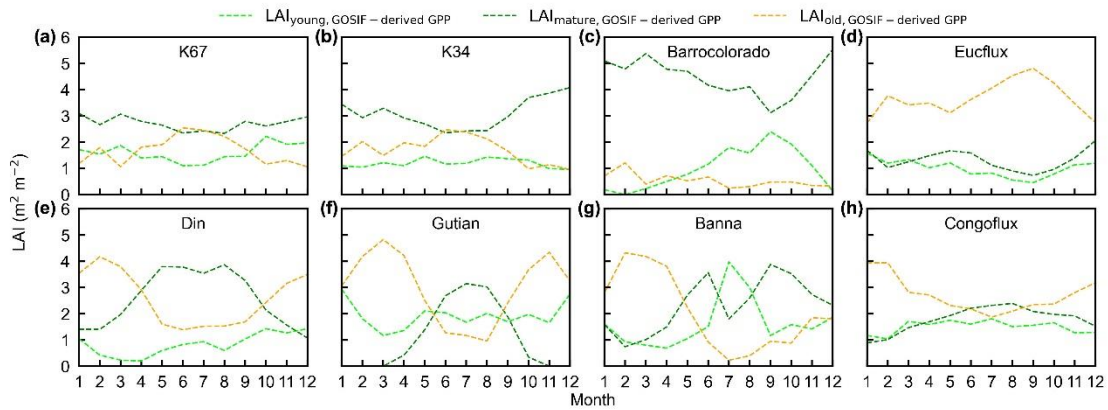
582 4*4 based on neighboring pixels. Results show that the seasonality of LAI_{young} ,
 583 LAI_{mature} and LAI_{old} in the 0.5-degree Lad-LAI products based on 4*4 neighboring
 584 pixels are highly consistent with those of the 0.25-degree one based on 2*2 neighboring
 585 pixels across the whole tropical region (**Fig. 14**), with the correlation coefficients (R)
 586 being equaling to 0.63, 0.68 and 0.95, respectively (**Fig. S11**).



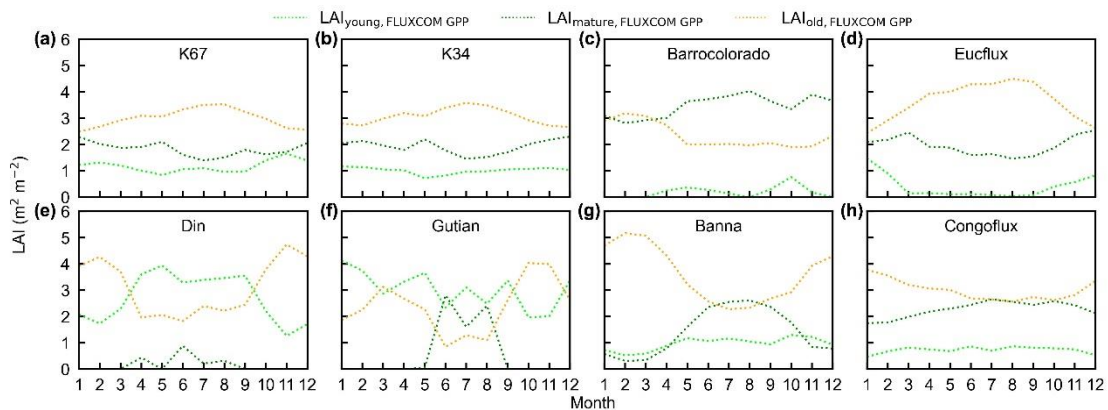
587
 588 **Figure 14.** The seasonality of LAI_{young} , LAI_{mature} , LAI_{old} between 0.25-degree and 0.5-
 589 degree Lad-LAI datasets in the 8 clustered regions. Limegreen color represents LAI_{young} ;
 590 green color represents LAI_{mature} ; and orange color represents LAI_{old} . Solid lines
 591 represent 0.25-degree dataset and the dashed lines represent 0.5-degree dataset.

592
 593 To test the uncertainties caused by the GPP estimation, we added two more GPP
 594 products, i.e., GOSIF-derived GPP (Li and Xiao, 2019) and FLUXCOM GPP (Jung et
 595 al., 2019), to produce another two versions of Lad-LAI products. The GPP seasonality
 596 coincide well between these three data sources across all the 8 sub-regions (**Fig. S12**).
 597 By comparing with the ground-based LAI cohorts at eight observation sites, results
 598 show that the Lad-LAI generated from RTSIF-derived GPP show highest correlation
 599 and minimal deviation with the *in situ* measurements, with R equaling to 0.36, 0.77 and
 600 0.59 and MSD equaling to 0.45, 0.69 and 0.62 for LAI_{young} , LAI_{mature} , and LAI_{old} ,

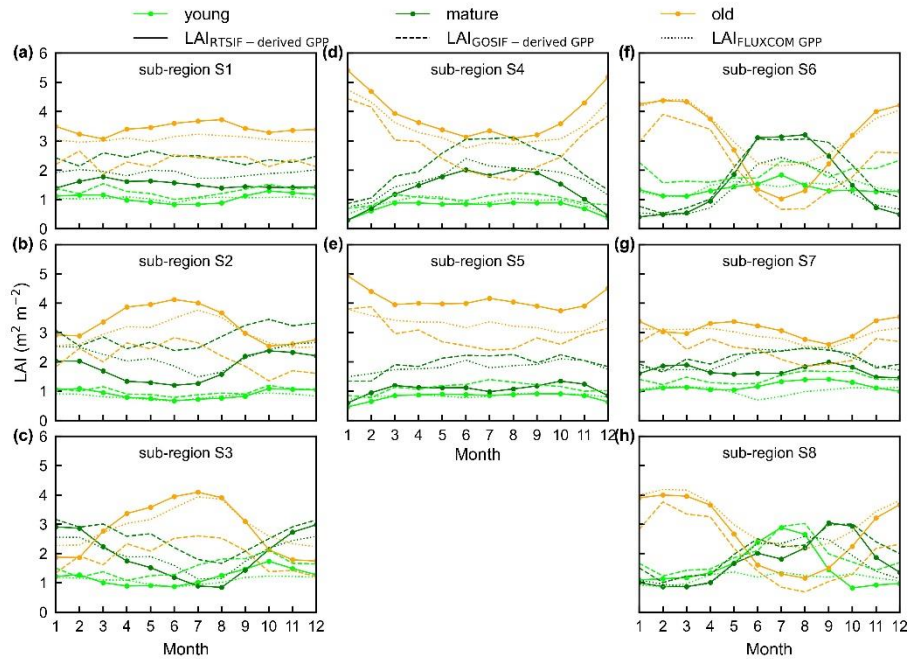
601 respectively (Figs. 15-16, S13-S15). Additionally, we also compared the seasonal
 602 variability of LAI_{young} , LAI_{mature} , and LAI_{old} between three Lad-LAI versions in 8 sub-
 603 regions classified by the K-means clustering analysis (Fig. 17). In general, three
 604 versions of Lad-LAI products all performed well in 8 sub-regions with the consistent
 605 seasonal variability (Fig. 17). On regional average, sub-regions S4, S5, S6, S7 and S8
 606 show high consistent seasonality of LAI_{young} , LAI_{mature} , and LAI_{old} between these three
 607 products; whereas the Lad-LAI generated from GOSIF-derived GPP performs a little
 608 poor in capturing the seasonality of LAI cohorts in Amazon (sub-regions S1, S2 and
 609 S3).



610
 611 **Figure 15.** Seasonality of simulated LAI_{young} , LAI_{mature} , and LAI_{old} from GOSIF-
 612 derived GPP in comparison with observed data at 8 sites. (a) K67; (b) K34; (c)
 613 Barrocolorado; (d) Eucflux; (e) Din; (f) Gutian; (g) Banna; (h) Congoflux.



614
 615 **Figure 16.** Seasonality of simulated LAI_{young} , LAI_{mature} , and LAI_{old} from FLUXCOM
 616 GPP in comparison with observed data at 8 sites. (a) K67; (b) K34; (c) Barrocolorado;
 617 (d) Eucflux; (e) Din; (f) Gutian; (g) Banna; (h) Congoflux.



618

619 **Figure 17.** Seasonality of simulated LAI_{young} , LAI_{mature} , and LAI_{old} from three version
 620 products in 8 sub-regions classified by the K-means clustering analysis. Solid lines
 621 represent LAI generated from RTSIF-derived GPP; dashed lines represent LAI
 622 generated from GOSIF-derived GPP; and dotted lines represent LAI generated from
 623 FLUXCOM GPP. Limegreen represents LAI_{young} ; green represents LAI_{mature} ; and
 624 orange represents LAI_{old} .

625

626 **5 Discussion**

627 Leaf age-dependent LAI performs well in describing the seasonal replacements of
 628 canopy leaves in TEFs (Wu et al., 2016; Chen et al., 2020), showing to be a critical
 629 plant trait for representing the tropical and subtropical phenology (Doughty and
 630 Goulden, 2008; Saleska et al., 2007). However, to our knowledge, there are currently
 631 no continental-scale information of such leaf age-dependent LAI data over the whole
 632 TEFs, as it can neither be mapped from sparse site observations (Wu et al., 2016), nor
 633 be modeled from ESMs which are triggered by unclear climatic drivers (Chen et al.,
 634 2020). These hinder global researches on accurately simulations of large-scale
 635 photosynthesis (GPP) seasonality using remote sensing approaches and ESMs (Chen et
 636 al., 2020).

637 The Lad-LAI product developed in this study is a new continental-scale grid dataset
638 of monthly LAI in different leaf age cohorts. Although lacking of enough *in situ*
639 observations for adequate validations, the seasonality of three LAI cohorts performs
640 well at the **eight** sites (**four in south America, three in subtropical Asia and one in Congo**)
641 with very **fine-scale** collections of monthly LAI_{young}, LAI_{mature}, and LAI_{old}. To test the
642 robustness of the grid Lad-LAI products over the whole TEFs, the seasonality of
643 LAI_{mature} seasonality are also validated pixel by pixel using satellite-based EVI products
644 and the phase of LAI_{old} seasonality are compared with the those of seasonal litterfall
645 data from 53 site measurements, respectively. Moreover, the LAI_{young+mature} from the
646 new Lad-LAI products can also directly represent the large-scale dry-season green-up
647 of canopy leaves north of the Equator. **Overall**, direct and indirect evaluations both
648 demonstrated the robustness of the **developed** Lad-LAI products.

649 It should be noted that, over the regions with large magnitude of annual
650 precipitation nearby the Equator, there is no obvious dry seasons and thus tree canopy
651 phenology changes smaller than higher-latitude ones throughout the year (Yang et al.,
652 2021). The LAI of young, mature and old leaf cohorts all show a bimodal phenology
653 with marginally small seasonal changes nearby the **Equator**, which is captured by the
654 developed Lad-LAI product. Secondly, we **used** a constant **coefficient** to transfer from
655 SIF data to GPP and also assume a constant value for the total LAI over the whole TEFs,
656 which **might** bring unexpected **uncertainties**. This can be seen from the MSD
657 evaluations, where the bias-related term **dominates** the total MSD, especially in regions
658 nearby the Equator. However, this bring less impacts on the seasonality of Lad-LAI, as
659 the phase-related term of MSD is much smaller.

660 Additionally, the maximum carboxylation rate ($V_{c,max}$) of leaves changes
661 significantly with leaf age (Xu et al., 2017). Currently, most Earth system models
662 (ESMs) define $V_{c,max}$ as a function of leaf age whereas their relationship is still less well
663 understood in TEFs due to sparse in-situ measurements (Chen et al., 2020). This
664 consequentially **leads to the poor** representation of LAI and GPP seasonality in ESMs

665 (De Weirdt et al., 2012). To overcome this challenge, **here** we simplified the tree canopy
666 into three big leaves (i.e., young, mature and old) in TEFs, similar as the two-big leaves
667 model developed for temperate and boreal forests (Best et al., 2011; Clark et al., 2011;
668 Harper et al., 2016), which simplified tree canopy into sun and shade leaves. However,
669 some uncertain remains on the assumption, as it neglects the spatial and temporal
670 variations of $V_{c,max}$, which also changes with seasonal climate anomaly and also differs
671 between nearby pixels in high heterogeneous forest ecosystems. This assumption may
672 bring uncertainties for simulating seasonal An and therefore influence the seasonality
673 of Lad-LAI.

674 In summary, we developed a new method to produce the first **global** grid dataset of
675 leaf age-dependent LAI product **across the whole EBFs** over the continental scale.
676 Although some uncertainties **might** remain, **the Lad-LAI products could provide**
677 **seasonal age-dependent LAI data at the pixel-level to develop a common phenology**
678 **model for the whole tropical and subtropical EBFs in** ESMS that are currently run at a
679 coarser resolution. **Besides, with** the development of remote sensing technology, finer
680 temporal and spatial resolutions of SIF products will enable finer temporal and spatial
681 resolutions maps of Lad-LAI products **in the future**.

682

683 **6. Data availability**

684 The 0.25-degree leaf age-dependent LAI seasonality (Lad-LAI) **data** from 2001-
685 2018 **are** presented in this paper **as the main one, and their time-series are as a**
686 **supplementary dataset. The two datasets are available at**
687 **<https://doi.org/10.6084/m9.figshare.21700955.v3>** (Yang et al., 2022). **Besides, we also**
688 **provided another two versions of Lad-LAI generated from GOSIF-derived GPP and**
689 **FLUXCOM GPP, respectively. These datasets are compressed in GeoTiff, with a spatial**
690 **reference of WGS84. Each file in those dataset is named like “LAI_{leaf age}_{spatial**
691 **resolution}_{month/year-month}.tif”.**

692

693 **7. Conclusion**

694 This study for the first-time mapped continental-scale grid dataset of monthly LAI
695 in three leaf age cohorts from 2001-2018 RTSIF data. The LAI seasonality of young,
696 mature and old leaves was evaluated using *in situ* measurements of seasonal LAI data,
697 satellite based EVI and *in situ* measurements of seasonal litterfall data. The evaluations
698 from these datasets demonstrate the robustness of the seasonality of three leaf age
699 cohorts. The new Lad-LAI products indicate diverse patterns over the whole tropical
700 and subtropical regions. In central and south Amazon, LAI_{young} and LAI_{mature} decrease
701 at early **dry** season around February and convert to increase at early wet season around
702 June. On the contrary, in subtropical Asia, LAI_{young} and LAI_{mature} increase during the
703 wet season and peak with largest rainfall at June or July. In regions nearby the Equator,
704 the LAI cohorts show a bimodal phenology but with marginally small changes in
705 magnitudes. The proposed method will enable to produce finer temporal and spatial
706 resolutions maps of Lad-LAI products by using precise temporal and spatial resolutions
707 data as the inputs. The Lad-LAI products will be help for diagnosing the adaption of
708 tropical and subtropical forest to climate change; and will also help improve the
709 development of phenology models in ESMs.

710

711 **Supplement.** The supplement related to this article will be available online at once
712 accepted.

713

714 **Author contributions.** XZ designed the research and wrote the paper. XY
715 performed the analyses. All the authors edited and revised the paper.

716

717 **Competing interests.** The authors declare no competing interests.

718

719 **Financial support.**

720 This study was supported by the National Natural Science Foundation of China

721 (grant numbers [U21A6001](#), 31971458, 41971275), the Guangdong Major Project of
722 Basic and Applied Basic Research (grant number 2020B0301030004), the Special high-
723 level plan project of Guangdong Province (grant number 2016TQ03Z354), Innovation
724 Group Project of Southern Marine Science and Engineering Guangdong Laboratory
725 (Zhuhai) (grant number 311021009).

726

727 **Acknowledgement**

728 Thanks for Dr. Jin Wu from Hongkong University for providing the observation
729 data of LAI cohorts at K67 and K34 sites in Amazon. We would also like to thank the
730 editor and reviewers for their valuable time in reviewing the manuscript.

731

732 **Reference:**

- 733 Albert, L. P., Wu, J., Prohaska, N., de Camargo, P. B., Huxman, T. E., Tribuzy, E. S.,
734 Ivanov, V. Y., Oliveira, R. S., Garcia, S., Smith, M. N., Oliveira Junior, R. C.,
735 Restrepo-Coupe, N., da Silva, R., Stark, S. C., Martins, G. A., Penha, D. V., and
736 Saleska, S. R.: Age-dependent leaf physiology and consequences for crown-scale
737 carbon uptake during the dry season in an Amazon evergreen forest, *New Phytol*,
738 219, 870-884, [10.1111/nph.15056](#), 2018.
- 739 Aragao, L. E., Poulter, B., Barlow, J. B., Anderson, L. O., Malhi, Y., Saatchi, S., Phillips,
740 O. L., and Gloor, E.: Environmental change and the carbon balance of Amazonian
741 forests, *Biol Rev Camb Philos Soc*, 89, 913-931, [10.1111/brv.12088](#), 2014.
- 742 Arora, V. K. and Boer, G. J.: Fire as an interactive component of dynamic vegetation
743 models, *Journal of Geophysical Research: Biogeosciences*, 110, n/a-n/a,
744 [10.1029/2005jg000042](#), 2005.
- 745 Barlow, J., Gardner, T. A., Ferreira, L. V., and Peres, C. A.: Litter fall and decomposition
746 in primary, secondary and plantation forests in the Brazilian Amazon, *Forest
747 Ecology and Management*, 247, 91-97, [10.1016/j.foreco.2007.04.017](#), 2007.
- 748 Beer, C., Reichstein, M., Tomelleri, E., Ciais, P., Jung, M., Carvalhais, N., Rodenbeck,
749 C., Arain, M. A., Baldocchi, D., Bonan, G. B., Bondeau, A., Cescatti, A., Lasslop,
750 G., Lindroth, A., Lomas, M., Luysaert, S., Margolis, H., Oleson, K. W., Rouspard,
751 O., Veenendaal, E., Viovy, N., Williams, C., Woodward, F. I., and Papale, D.:
752 Terrestrial gross carbon dioxide uptake: global distribution and covariation with
753 climate, *Science*, 329, 834-838, [10.1126/science.1184984](#), 2010.
- 754 Bernacchi, C. J., Pimentel, C., and Long, S. P.: In vivo temperature response functions
755 of parameters required to model RuBP-limited photosynthesis, *Plant, Cell &
756 Environment*, 26, 1419-1430, [10.1046/j.0016-8025.2003.01050.x](#), 2003.

757 Bernacchi, C. J., Bagley, J. E., Serbin, S. P., Ruiz-Vera, U. M., Rosenthal, D. M., and
758 Vanloocke, A.: Modelling C(3) photosynthesis from the chloroplast to the
759 ecosystem, *Plant Cell Environ*, 36, 1641-1657, 10.1111/pce.12118, 2013.

760 Best, M. J., Pryor, M., Clark, D. B., Rooney, G. G., Essery, R. L. H., Ménard, C. B.,
761 Edwards, J. M., Hendry, M. A., Porson, A., Gedney, N., Mercado, L. M., Sitch, S.,
762 Blyth, E., Boucher, O., Cox, P. M., Grimmond, C. S. B., and Harding, R. J.: The
763 Joint UK Land Environment Simulator (JULES), model description–Part 1:
764 Energy and water fluxes. *Geoscientific Model Development*, 4, 677–699, 2011.

765 Brando, P. M., Goetz, S. J., Baccini, A., Nepstad, D. C., Beck, P. S., and Christman, M.
766 C.: Seasonal and interannual variability of climate and vegetation indices across
767 the Amazon. *Proceedings of the National Academy of Sciences*, 200908741. 2010.

768 Chen, X., Huang, Y., Nie, C., Zhang, S., Wang, G., Chen, S., and Chen, Z.: A long-term
769 reconstructed TROPOMI solar-induced fluorescence dataset using machine
770 learning algorithms, *Sci Data*, 9, 427, 10.1038/s41597-022-01520-1, 2022.

771 Chen, X., Maignan, F., Viovy, N., Bastos, A., Goll, D., Wu, J., Liu, L., Yue, C., Peng,
772 S., Yuan, W., Conceição, A. C., O'Sullivan, M., and Ciais, P.: Novel Representation
773 of Leaf Phenology Improves Simulation of Amazonian Evergreen Forest
774 Photosynthesis in a Land Surface Model, *Journal of Advances in Modeling Earth
775 Systems*, 12, 10.1029/2018ms001565, 2020.

776 Chen, X., Ciais, P., Maignan, F., Zhang, Y., Bastos, A., Liu, L., Bacour, C., Fan, L.,
777 Gentine, P., Goll, D., Green, J., Kim, H., Li, L., Liu, Y., Peng, S., Tang, H., Viovy,
778 N., Wigneron, J. P., Wu, J., Yuan, W., and Zhang, H.: Vapor Pressure Deficit and
779 Sunlight Explain Seasonality of Leaf Phenology and Photosynthesis Across
780 Amazonian Evergreen Broadleaved Forest, *Global Biogeochemical Cycles*, 35,
781 10.1029/2020gb006893, 2021.

782 Clark, D. B., Mercado, L. M., Sitch, S., Jones, C. D., Gedney, N., Best, M. J., Pryor,
783 M., Rooney, G. G., Essery, R. L. H., Blyth, E., Boucher, O., Harding, R. J.,
784 Huntingford, C., and Cox, P. M.: The Joint UK Land Environment Simulator
785 (JULES), model description–Part 2: Carbon fluxes and vegetation dynamics.
786 *Geoscientific Model Development*, 4, 701–722, 2011.

787 Cramer, W., Bondeau, A., Woodward, F. I., Prentice, I. C., Betts, R. A., Brovkin, V.,
788 Cox, P. M., Fisher, V., Foley, J. A., Friend, A. D., Kucharik, C., Lomas, M. R.,
789 Ramankutty, N., Sitch, S., Smith, B., White, A., and Young-Molling, C.: Global
790 response of terrestrial ecosystem structure and function to CO₂ and climate change:
791 results from six dynamic global vegetation models, *Global Change Biology*, 7,
792 357-373, 10.1046/j.1365-2486.2001.00383.x, 2001.

793 Dantas, M. and Phillipson, J.: Litterfall and litter nutrient content in primary and
794 secondary Amazonian ‘terra firme’ rain forest, *Journal of Tropical Ecology*, 5, 27-

795 36, 10.1017/s0266467400003199, 1989.

796 Davidson, E. A., de Araújo, A. C., Balch, J. K., Brown, I. F., Bustamante, M. M., et al.:

797 The Amazon basin in transition. *Nature*, 481(7381), 321–328.

798 <https://doi.org/10.1038/nature10717>. 2012.

799 de Moura, Y. M., Galvão, L. S., Hilker, T., Wu, J., Saleska, S., do Amaral, C. H., Nelson,

800 B. W., Lopes, A. P., Wiedeman, K. K., Prohaska, N., de Oliveira, R. C., Machado,

801 C. B., and Aragão, L. E. O. C.: Spectral analysis of amazon canopy phenology

802 during the dry season using a tower hyperspectral camera and modis observations,

803 *ISPRS Journal of Photogrammetry and Remote Sensing*, 131, 52–64,

804 10.1016/j.isprsjprs.2017.07.006, 2017.

805 De Weirdt, M., Verbeeck, H., Maignan, F., Peylin, P., Poulter, B., Bonal, D., Ciais, P.,

806 and Steppe, K.: Seasonal leaf dynamics for tropical evergreen forests in a process-

807 based global ecosystem model, *Geoscientific Model Development*, 5, 1091–1108,

808 10.5194/gmd-5-1091-2012, 2012.

809 Dechant, B., Ryu, Y., Badgley, G., Zeng, Y., Berry, J. A., Zhang, Y., Goulas, Y., Li, Z.,

810 Zhang, Q., Kang, M., Li, J., and Moya, I.: Canopy structure explains the

811 relationship between photosynthesis and sun-induced chlorophyll fluorescence in

812 crops, *Remote Sensing of Environment*, 241, 10.1016/j.rse.2020.111733, 2020.

813 Dee, D. P., Uppala, S. M., Simmons, A. J., Berrisford, P., Poli, P., Kobayashi, S., Andrae,

814 U., Balmaseda, M. A., Balsamo, G., Bauer, P., Bechtold, P., Beljaars, A. C. M., van

815 de Berg, L., Bidlot, J., Bormann, N., Delsol, C., Dragani, R., Fuentes, M., Geer, A.

816 J., Haimberger, L., Healy, S. B., Hersbach, H., Hólm, E. V., Isaksen, L., Kållberg,

817 P., Köhler, M., Matricardi, M., McNally, A. P., Monge-Sanz, B. M., Morcrette, J.

818 J., Park, B. K., Peubey, C., de Rosnay, P., Tavolato, C., Thépaut, J. N., and Vitart,

819 F.: The ERA-Interim reanalysis: configuration and performance of the data

820 assimilation system, *Quarterly Journal of the Royal Meteorological Society*, 137,

821 553–597, 10.1002/qj.828, 2011.

822 Doughty, C. E. and Goulden, M. L.: Seasonal patterns of tropical forest leaf area index

823 and CO₂ exchange, *Journal of Geophysical Research: Biogeosciences*, 113, n/a-

824 n/a, 10.1029/2007jg000590, 2008.

825 Farquhar, G. D., von Caemmerer, S., and Berry, J. A.: A biochemical model of

826 photosynthetic CO₂ assimilation in leaves of C₃ species, *Planta*, 149, 78–90,

827 10.1007/BF00386231, 1980.

828 Galvão, L. S., dos Santos, J. R., Roberts, D. A., Breunig, F. M., Toomey, M., and de

829 Moura, Y. M.: On intra-annual EVI variability in the dry season of tropical forest:

830 a case study with MODIS and hyperspectral data. *Remote Sens. Environ.* 115,

831 2350–2359, 2011.

832 Guan, K., Berry, J. A., Zhang, Y., Joiner, J., Guanter, L., Huete, A. R., ... and Gentine,

833 P.: Improving the monitoring of crop productivity using spaceborne solar-induced

834 fluorescence. *Global change biology*, 22(2), 716–726. 2016.

835 Guan, K., Pan, M., Li, H., Wolf, A., Wu, J., Medvigy, D., Caylor, K. K., Sheffield, J.,

836 Wood, E. F., Malhi, Y., Liang, M., Kimball, J. S., Saleska, Scott R., Berry, J., Joiner,

837 J., and Lyapustin, A. I.: Photosynthetic seasonality of global tropical forests
838 constrained by hydroclimate, *Nature Geoscience*, 8, 284-289, 10.1038/ngeo2382,
839 2015.

840 Harper, A., Cox, P., Friedlingstein, P., Wiltshire, A. J., Jones, C. D., Sitch, S., . . . van
841 Bodegom, P.: Improved representation of plant functional types and physiology in
842 the Joint UK Land Environment Simulator (JULES v4.2) using plant trait
843 information. *Geoscientific Model Development Discussions*, 9, 2415–2440, 2016.

844 Huete, A., Didan, K., Miura, T., Rodriguez, E. P., Gao, X., and Ferreira, L. G.: Overview
845 of the radiometric and biophysical performance of the MODIS vegetation indices,
846 *Remote Sensing of Environment*, 83, 195-213, 10.1016/s0034-4257(02)00096-2,
847 2002.

848 Huete, A. R., Didan, K., Shimabukuro, Y. E., Ratana, P., Saleska, S. R., Hutyrá, L. R.,
849 Yang, W., Nemani, R. R., and Myneni, R.: Amazon rainforests green-up with
850 sunlight in dry season, *Geophysical Research Letters*, 33, 10.1029/2005gl025583,
851 2006.

852 June, T., Evans, J. R., and Farquhar, G. D.: A simple new equation for the reversible
853 temperature dependence of photosynthetic electron transport: a study on soybean
854 leaf, *Funct Plant Biol*, 31, 275-283, 10.1071/FP03250, 2004.

855 Jung, M., Koirala, S., Weber, U., Ichii, K., Gans, F., Camps-Valls, G., Papale, D.,
856 Schwalm, C., Tramontana, G., and Reichstein, M.: The FLUXCOM ensemble of
857 global land-atmosphere energy fluxes. *Sci Data* 6, 74.
858 <https://doi.org/10.1038/s41597-019-0076-8>. 2019.

859 Kartikeyan, B., Sarkar, A., and Majumder, K. L.: A segmentation approach to
860 classification of remote sensing imagery, *International Journal of Remote Sensing*,
861 19, 1695-1709, 1998.

862 Kobayashi, K. and Salam, M. U.: Comparing Simulated and Measured Values Using
863 Mean Squared Deviation and its Components, *Agronomy Journal*, 92,
864 10.1007/s100870050043, 2000.

865 Leff, J. W., Wieder, W. R., Taylor, P. G., Townsend, A. R., Nemergut, D. R., Grandy, A.
866 S., and Cleveland, C. C.: Experimental litterfall manipulation drives large and
867 rapid changes in soil carbon cycling in a wet tropical forest. *Global Change*
868 *Biology*, 18(9), 2969–2979. <https://doi.org/10.1111/j.1365-2486.2012.02749.x>.
869 2012.

870 Li, Q., Chen, X., Yuan, W., Lu, H., Shen, R., Wu, S., Gong, F., Dai, Y., Liu, L., Sun, Q.,
871 Zhang, C., and Su, Y.: Remote Sensing of Seasonal Climatic Constraints on Leaf
872 Phenology Across Pantropical Evergreen Forest Biome, *Earth's Future*, 9,
873 10.1029/2021ef002160, 2021.

874 Li, X., and Xiao, J.: Mapping photosynthesis solely from solar-induced chlorophyll
875 fluorescence: A global, fine-resolution dataset of gross primary production derived
876 from OCO-2. *Remote Sensing*, 11(21), 2563; <https://doi.org/10.3390/rs11212563>.
877 2019.

878 Lin, Y.-S., Medlyn, B. E., Duursma, R. A., Prentice, I. C., Wang, H., Baig, S., Eamus,

879 D., de Dios, Victor R., Mitchell, P., Ellsworth, D. S., de Beeck, M. O., Wallin, G.,
880 Uddling, J., Tarvainen, L., Linderson, M.-L., Cernusak, L. A., Nippert, J. B.,
881 Ocheltree, T. W., Tissue, D. T., Martin-StPaul, N. K., Rogers, A., Warren, J. M.,
882 De Angelis, P., Hikosaka, K., Han, Q., Onoda, Y., Gimeno, T. E., Barton, C. V. M.,
883 Bennie, J., Bonal, D., Bosc, A., Löw, M., Macinins-Ng, C., Rey, A., Rowland, L.,
884 Setterfield, S. A., Tausz-Posch, S., Zaragoza-Castells, J., Broadmeadow, M. S. J.,
885 Drake, J. E., Freeman, M., Ghannoum, O., Hutley, Lindsay B., Kelly, J. W.,
886 Kikuzawa, K., Kolari, P., Koyama, K., Limousin, J.-M., Meir, P., Lola da Costa,
887 A. C., Mikkelsen, T. N., Salinas, N., Sun, W., and Wingate, L.: Optimal stomatal
888 behaviour around the world, *Nature Climate Change*, 5, 459-464,
889 10.1038/nclimate2550, 2015.

890 Lopes, A. P., Nelson, B. W., Wu, J., Graça, P. M. L. d. A., Tavares, J. V., Prohaska, N.,
891 Martins, G. A., and Saleska, S. R.: Leaf flush drives dry season green-up of the
892 Central Amazon, *Remote Sensing of Environment*, 182, 90-98,
893 10.1016/j.rse.2016.05.009, 2016.

894 Maes, W. H., Gentine, P., Verhoest, N. E. C., and Miralles, D. G.: Potential evaporation
895 at eddy-covariance sites across the globe, *Hydrology and Earth System Sciences*,
896 23, 925-948, 10.5194/hess-23-925-2019, 2019.

897 Medlyn, B. E., Duursma, R. A., Eamus, D., Ellsworth, D. S., Prentice, I. C., Barton, C.
898 V. M., Crous, K. Y., De Angelis, P., Freeman, M., and Wingate, L.: Reconciling
899 the optimal and empirical approaches to modelling stomatal conductance, *Global
900 Change Biology*, 17, 2134-2144, 10.1111/j.1365-2486.2010.02375.x, 2011.

901 **Melgosa, M., Huertas, R., and Berns, R. S.: Performance of recent advanced color-
902 difference formulas using the standardized residual sum of squares index. *Journal
903 of the Optical Society of America A*, 25(7), 1828-1834.
904 <https://doi.org/10.1364/JOSAA.25.001828>. 2008**

905 **Menezes, J., Garcia, S., Grandis, A., Nascimento, H., Domingues, T. F., Guedes, A. V.,
906 Aleixo, I., Camargo, P., Campos, J., Damasceno, A., Dias-Silva, R., Fleischer, K.,
907 Kruijt, B., Cordeiro, A. L., Martins, N. P., Meir, P., Norby, R. J., Pereira, I., Portela,
908 B., Rammig, A., Ribeiro, A. G., Lapola, D. M., and Quesada, C. A.: Changes in
909 leaf functional traits with leaf age: when do leaves decrease their photosynthetic
910 capacity in Amazonian trees? *Tree Physiology*, 42(5), 922-938,
911 <https://doi.org/10.1093/treephys/tpab042>, 2021.**

912 Merkl, R. and Waack, S.: *Bioinformatik interaktiv*, John Wiley & Sons, 2009.

913 Midoko Iponga, D., Mpikou, R. G. J., Loumeto, J., and Picard, N.: The effect of
914 different anthropogenic disturbances on litterfall of a dominant pioneer rain forest
915 tree in Gabon, *African Journal of Ecology*, 58, 281-290, 10.1111/aje.12696, 2019.

916 **Myneni, R. B., Yang, W., Nemani, R. R., Huete, A. R., Dickinson, R. E., Knyazikhin,
917 Y., Didan, K., Fu, R., Negrón Juárez, R. I., Saatchi, S. S., Hashimoto, H., Ichii, K.,
918 Shabanov, N. V., Tan, B., Ratana, P., Privette, J. L., Morisette, J. T., Vermote, E. F.,
919 Roy, D. P., Wolfe, R. E., Friedl, M. A., Running, S. W., Votava, P., El-Saleous, N.,
920 Devadiga, S., Su, Y., and Salomonson, V. V.: Large seasonal swings in leaf area of**

921 [Amazon rainforests. Proc. Natl Acad. Sci. USA, 104, 4820–4823. 2007.](#)

922 Ndakara, O. E.: Litterfall and Nutrient Returns in Isolated Stands of *Persea gratissima*

923 (Avocado Pear) in the Rainforest Zone of Southern Nigeria, *Ethiopian Journal of*

924 *Environmental Studies and Management*, 4, 10.4314/ejesm.v4i3.6, 2011.

925 Pastorello, G., Trotta, C., Canfora, E., Chu, H., Christianson, D., Cheah, Y. W.,

926 Poindexter, C., Chen, J., Elbashandy, A., Humphrey, M., Isaac, P., Polidori, D.,

927 Reichstein, M., Ribeca, A., van Ingen, C., Vuichard, N., Zhang, L., Amiro, B.,

928 Ammann, C., Arain, M. A., Ardo, J., Arkebauer, T., Arndt, S. K., Arriga, N.,

929 Aubinet, M., Aurela, M., Baldocchi, D., Barr, A., Beamesderfer, E., Marchesini, L.

930 B., Bergeron, O., Beringer, J., Bernhofer, C., Berveiller, D., Billesbach, D., Black,

931 T. A., Blanken, P. D., Bohrer, G., Boike, J., Bolstad, P. V., Bonal, D., Bonnefond,

932 J. M., Bowling, D. R., Bracho, R., Brodeur, J., Brummer, C., Buchmann, N.,

933 Burban, B., Burns, S. P., Buysse, P., Cale, P., Cavagna, M., Cellier, P., Chen, S.,

934 Chini, I., Christensen, T. R., Cleverly, J., Collalti, A., Consalvo, C., Cook, B. D.,

935 Cook, D., Coursolle, C., Cremonese, E., Curtis, P. S., D'Andrea, E., da Rocha, H.,

936 Dai, X., Davis, K. J., Cinti, B., Grandcourt, A., Ligne, A., De Oliveira, R. C.,

937 Delpierre, N., Desai, A. R., Di Bella, C. M., Tommasi, P. D., Dolman, H., Domingo,

938 F., Dong, G., Dore, S., Duce, P., Dufrene, E., Dunn, A., Dusek, J., Eamus, D.,

939 Eichelmann, U., ElKhidir, H. A. M., Eugster, W., Ewenz, C. M., Ewers, B.,

940 Famulari, D., Fares, S., Feigenwinter, I., Feitz, A., Fensholt, R., Filippa, G.,

941 Fischer, M., Frank, J., Galvagno, M., Gharun, M., Gianelle, D., Gielen, B., Gioli,

942 B., Gitelson, A., Goded, I., Goeckede, M., Goldstein, A. H., Gough, C. M.,

943 Goulden, M. L., Graf, A., Griebel, A., Gruening, C., Grunwald, T., Hammerle, A.,

944 Han, S., Han, X., Hansen, B. U., Hanson, C., Hatakka, J., He, Y., Hehn, M.,

945 Heinesch, B., Hinko-Najera, N., Hortnagl, L., Hutley, L., Ibrom, A., Ikawa, H.,

946 Jackowicz-Korczynski, M., Janous, D., Jans, W., Jassal, R., Jiang, S., Kato, T.,

947 Khomik, M., Klatt, J., Knohl, A., Knox, S., Kobayashi, H., Koerber, G., Kolle, O.,

948 Kosugi, Y., Kotani, A., Kowalski, A., Kruijt, B., Kurbatova, J., Kutsch, W. L.,

949 Kwon, H., Launiainen, S., Laurila, T., Law, B., Leuning, R., Li, Y., Liddell, M.,

950 Limousin, J. M., Lion, M., Liska, A. J., Lohila, A., Lopez-Ballesteros, A., Lopez-

951 Blanco, E., Loubet, B., Loustau, D., Lucas-Moffat, A., Luers, J., Ma, S.,

952 Macfarlane, C., Magliulo, V., Maier, R., Mammarella, I., Manca, G., Marcolla, B.,

953 Margolis, H. A., Marras, S., Massman, W., Mastepanov, M., Matamala, R.,

954 Matthes, J. H., Mazzenga, F., McCaughey, H., McHugh, I., McMillan, A. M. S.,

955 Merbold, L., Meyer, W., Meyers, T., Miller, S. D., Minerbi, S., Moderow, U.,

956 Monson, R. K., Montagnani, L., Moore, C. E., Moors, E., Moreaux, V., Moureaux,

957 C., Munger, J. W., Nakai, T., Neirynek, J., Nesic, Z., Nicolini, G., Noormets, A.,

958 Northwood, M., Noretto, M., Nouvellon, Y., Novick, K., Oechel, W., Olesen, J. E.,

959 Ourcival, J. M., Papuga, S. A., Parmentier, F. J., Paul-Limoges, E., Pavelka, M.,

960 Peichl, M., Pendall, E., Phillips, R. P., Pilegaard, K., Pirk, N., Posse, G., Powell,

961 T., Prasse, H., Prober, S. M., Rambal, S., Rannik, U., Raz-Yaseef, N., Reibmann,

962 C., Reed, D., Dios, V. R., Restrepo-Coupe, N., Reverter, B. R., Roland, M.,

963 Sabbatini, S., Sachs, T., Saleska, S. R., Sanchez-Canete, E. P., Sanchez-Mejia, Z.
964 M., Schmid, H. P., Schmidt, M., Schneider, K., Schrader, F., Schroder, I., Scott, R.
965 L., Sedlak, P., Serrano-Ortiz, P., Shao, C., Shi, P., Shironya, I., Siebicke, L., Sigut,
966 L., Silberstein, R., Sirca, C., Spano, D., Steinbrecher, R., Stevens, R. M.,
967 Sturtevant, C., Suyker, A., Tagesson, T., Takanashi, S., Tang, Y., Tapper, N., Thom,
968 J., Tomassucci, M., Tuovinen, J. P., Urbanski, S., Valentini, R., van der Molen, M.,
969 van Gorsel, E., van Huissteden, K., Varlagin, A., Verfaillie, J., Vesala, T., Vincke,
970 C., Vitale, D., Vygodskaya, N., Walker, J. P., Walter-Shea, E., Wang, H., Weber, R.,
971 Westermann, S., Wille, C., Wofsy, S., Wohlfahrt, G., Wolf, S., Woodgate, W., Li,
972 Y., Zampedri, R., Zhang, J., Zhou, G., Zona, D., Agarwal, D., Biraud, S., Torn, M.,
973 and Papale, D.: The FLUXNET2015 dataset and the ONEFlux processing pipeline
974 for eddy covariance data, *Sci Data*, 7, 225, 10.1038/s41597-020-0534-3, 2020.

975 **Pan, Y., Birdsey, R. A., Fang, J., Houghton, R., Kauppi, P. E., Kurz, W. A., et al.: A large**
976 **and persistent carbon sink in the world's forests. *Science*, 333(6045), 988–993.**
977 **<https://doi.org/10.1126/science.1201609>, 2011.**

978 Pearson, K.: VII. Mathematical contributions to the theory of evolution.—III.
979 Regression, heredity, and panmixia, *Philosophical Transactions of the Royal*
980 *Society of London. Series A, Containing Papers of a Mathematical or Physical*
981 *Character*, 187, 253-318, 10.1098/rsta.1896.0007, 1896.

982 **Piao, S., Fang, J., Zhou, L., Ciais, P. and Zhu, B.: Variations in satellite-derived**
983 **phenology in China's temperate vegetation. *Global Change Biology*, 12: 672-685.**
984 **<https://doi.org/10.1111/j.1365-2486.2006.01123.x>. 2006.**

985 Restrepo-Coupe, N., Levine, N. M., Christoffersen, B. O., Albert, L. P., Wu, J., Costa,
986 M. H., Galbraith, D., Imbuzeiro, H., Martins, G., da Araujo, A. C., Malhi, Y. S.,
987 Zeng, X., Moorcroft, P., and Saleska, S. R.: Do dynamic global vegetation models
988 capture the seasonality of carbon fluxes in the Amazon basin? A data-model
989 intercomparison, *Glob Chang Biol*, 23, 191-208, 10.1111/gcb.13442, 2017.

990 Ryu, Y., Baldocchi, D. D., Kobayashi, H., van Ingen, C., Li, J., Black, T. A., Beringer,
991 J., van Gorsel, E., Knohl, A., Law, B. E., and Rouspard, O.: Integration of MODIS
992 land and atmosphere products with a coupled-process model to estimate gross
993 primary productivity and evapotranspiration from 1 km to global scales, *Global*
994 *Biogeochemical Cycles*, 25, n/a-n/a, 10.1029/2011gb004053, 2011.

995 **Ryu, Y., Jiang, C., Kobayashi, H., and Detto, M.: MODIS-derived global land products**
996 **of shortwave radiation and diffuse and total photosynthetically active radiation at**
997 **5 km resolution from 2000, *Remote Sensing of Environment*, 204, 812-825,**
998 **[10.1016/j.rse.2017.09.021](https://doi.org/10.1016/j.rse.2017.09.021), 2018.**

999 Saatchi, S. S., Harris, N. L., Brown, S., Lefsky, M., Mitchard, E. T., Salas, W., Zutta, B.
1000 R., Buermann, W., Lewis, S. L., Hagen, S., Petrova, S., White, L., Silman, M., and
1001 Morel, A.: Benchmark map of forest carbon stocks in tropical regions across three
1002 continents, *Proc Natl Acad Sci U S A*, 108, 9899-9904, 10.1073/pnas.1019576108,
1003 2011.

1004 Saleska, S. R., Didan, K., Huete, A. R., and da Rocha, H. R.: Amazon forests green-up

1005 during 2005 drought, *Science*, 318, 612, 10.1126/science.1146663, 2007.

1006 Saleska, S. R., Wu, J., Guan, K., Araujo, A. C., Huete, A., Nobre, A. D., and Restrepo-
1007 Coupe, N.: Dry-season greening of Amazon forests, *Nature*, 531, E4-5,
1008 10.1038/nature16457, 2016.

1009 Saleska, S. R., Miller, S. D., Matross, D. M., Goulden, M. L., Wofsy, S. C., da Rocha,
1010 H. R., de Camargo, P. B., Crill, P., Daube, B. C., de Freitas, H. C., Hutyrá, L.,
1011 Keller, M., Kirchhoff, V., Menton, M., Munger, J. W., Pyle, E. H., Rice, A. H., and
1012 Silva, H.: Carbon in Amazon forests: unexpected seasonal fluxes and disturbance-
1013 induced losses, *Science*, 302, 1554-1557, 10.1126/science.1091165, 2003.

1014 Sayer, E. J., Heard, M. S., Grant, H. K., Marthews, T. R., and Tanner, E. V. J.: Soil
1015 carbon release enhanced by increased tropical forest litterfall. *Nature Climate*
1016 *Change*, 1(6), 304–307. <https://doi.org/10.1038/nclimate1190>. 2011.

1017 Smith, M. N., Stark, S. C., Taylor, T. C., Ferreira, M. L., de Oliveira, E., Restrepo-
1018 Coupe, N., Chen, S., Woodcock, T., dos Santos, D. B., Alves, L. F., Figueira, M.,
1019 de Camargo, P. B., de Oliveira, R. C., Aragão, L. E. O. C., Falk, D. A., McMahon,
1020 S. M., Huxman, T. E. and Saleska, S. R.: Seasonal and drought-related changes in
1021 leaf area profiles depend on height and light environment in an Amazon forest.
1022 *New Phytol*, 222: 1284-1297. <https://doi.org/10.1111/nph.15726>. 2019.

1023 Sulla-Menashe, D., Woodcock, C. E., and Friedl, M. A.: Canadian boreal forest
1024 greening and browning trends: An analysis of biogeographic patterns and the
1025 relative roles of disturbance versus climate drivers. *Environmental Research*
1026 *Letters*, 13(1), 014007, 2018.

1027 Tang, H., and Dubayah, R.: Light-driven growth in Amazon evergreen forests explained
1028 by seasonal variations of vertical canopy structure. *Proceedings of the National*
1029 *Academy of Sciences of the United States of America*, 114(10), 2640–2644.
1030 <https://doi.org/10.1073/pnas.1616943114>. 2017.

1031 Toomey, M., Roberts, D. A. and Nelson, B.: The influence of epiphylls on remote
1032 sensing of humid forests. *Remote Sens. Environ*, 113, 1787–1798. 2009.

1033 Wang, C., Li, J., Liu, Q., Zhong, B., Wu, S., and Xia, C.: Analysis of Differences in
1034 Phenology Extracted from the Enhanced Vegetation Index and the Leaf Area Index,
1035 *Sensors (Basel)*, 17, 10.3390/s17091982, 2017.

1036 Weiss, A. and Norman, J. M.: Partitioning solar radiation into direct and diffuse, visible
1037 and near-infrared components, *Agricultural and Forest Meteorology*, 34, 205-213,
1038 10.1016/0168-1923(85)90020-6, 1985.

1039 Wu, J., Serbin, S. P., Xu, X., Albert, L. P., Chen, M., Meng, R., Saleska, S. R., and
1040 Rogers, A.: The phenology of leaf quality and its within-canopy variation is
1041 essential for accurate modeling of photosynthesis in tropical evergreen forests,
1042 *Glob Chang Biol*, 23, 4814-4827, 10.1111/gcb.13725, 2017.

1043 Wu, J., Kobayashi, H., Stark, S. C., Meng, R., Guan, K., Tran, N. N., Gao, S., Yang, W.,
1044 Restrepo-Coupe, N., Miura, T., Oliviera, R. C., Rogers, A., Dye, D. G., Nelson, B.
1045 W., Serbin, S. P., Huete, A. R., and Saleska, S. R.: Biological processes dominate
1046 seasonality of remotely sensed canopy greenness in an Amazon evergreen forest,

1047 New Phytol, 217, 1507-1520, 10.1111/nph.14939, 2018.

1048 Wu, J., Albert, L. P., Lopes, A. P., Restrepo-Coupe, N., Hayek, M., Wiedemann, K. T.,
1049 Guan, K., Stark, S. C., Christoffersen, B., Prohaska, N., Tavares, J. V., Marostica,
1050 S., Kobayashi, H., Ferreira, M. L., Campos, K. S., da Silva, R., Brando, P. M., Dye,
1051 D. G., Huxman, T. E., Huete, A. R., Nelson, B. W., and Saleska, S. R.: Leaf
1052 development and demography explain photosynthetic seasonality in Amazon
1053 evergreen forests, *Science*, 351, 972-976, 10.1126/science.aad5068, 2016.

1054 Xiao, X., Zhang, Q., Saleska, S., Hutyrá, L., De Camargo, P., Wofsy, S., Frolking, S.,
1055 Boles, S., Keller, M., and Moore, B.: Satellite-based modeling of gross primary
1056 production in a seasonally moist tropical evergreen forest, *Remote Sensing of
1057 Environment*, 94, 105-122, 10.1016/j.rse.2004.08.015, 2005.

1058 Xu, L., Saatchi, S. S., Yang, Y., Myneni, R. B., Frankenberg, C., Chowdhury, D., and
1059 Bi, J.: Satellite observation of tropical forest seasonality: spatial patterns of carbon
1060 exchange in Amazonia, *Environmental Research Letters*, 10, 10.1088/1748-
1061 9326/10/8/084005, 2015.

1062 Xu, X., Medvigy, D., Joseph Wright, S., Kitajima, K., Wu, J., Albert, L. P., Martins, G.
1063 A., Saleska, S. R., and Pacala, S. W.: Variations of leaf longevity in tropical moist
1064 forests predicted by a trait-driven carbon optimality model, *Ecol Lett*, 20, 1097-
1065 1106, 10.1111/ele.12804, 2017.

1066 Yang, X., Tang, J., Mustard, J. F., Lee, J.-E., Rossini, M., Joiner, J., Munger, J. W.,
1067 Kornfeld, A., and Richardson, A. D.: Solar-induced chlorophyll fluorescence that
1068 correlates with canopy photosynthesis on diurnal and seasonal scales in a
1069 temperate deciduous forest, *Geophysical Research Letters*, 42, 2977-2987,
1070 10.1002/2015gl063201, 2015.

1071 Yang, X., Wu, J., Chen, X., Ciais, P., Maignan, F., Yuan, W., Piao, S., Yang, S., Gong,
1072 F., Su, Y., Dai, Y., Liu, L., Zhang, H., Bonal, D., Liu, H., Chen, G., Lu, H., Wu, S.,
1073 Fan, L., Gentile, P., and Wright, S. J.: A comprehensive framework for seasonal
1074 controls of leaf abscission and productivity in evergreen broadleaved tropical and
1075 subtropical forests, *Innovation (Camb)*, 2, 100154, 10.1016/j.xinn.2021.100154,
1076 2021.

1077 Yang, X., Chen, X., Ren, J., Yuan, W., Liu, L., Liu, J., Chen, D., Xiao, Y., Wu, S., Fan,
1078 L., Dai, X., Su, Y.: Leaf age-dependent LAI seasonality product (Lad-LAI) over
1079 tropical and subtropical evergreen broadleaved forests. figshare. Dataset.
1080 <https://doi.org/10.6084/m9.figshare.21700955.v3>. 2022.

1081 Yuan, W., Zheng, Y., Piao, S., Ciais, P., Lombardozzi, D., Wang, Y., Ryu, Y., Chen, G.,
1082 Dong, W., Hu, Z., Jain, A. K., Jiang, C., Kato, E., Li, S., Lienert, S., Liu, S., Nabel,
1083 J., Qin, Z., Quine, T., Sitch, S., Smith, W. K., Wang, F., Wu, C., Xiao, Z., and Yang,
1084 S.: Increased atmospheric vapor pressure deficit reduces global vegetation growth,
1085 *Sci Adv*, 5, eaax1396, 10.1126/sciadv.aax1396, 2019.

1086 Zhao, P., Gao, L., Wei, J., Ma, M., Deng, H., Gao, J., and Chen, X.: Evaluation of ERA-
1087 Interim Air Temperature Data over the Qilian Mountains of China. *Advances in
1088 Meteorology*, 7353482. <https://doi.org/10.1155/2020/7353482>, 2020